

# Implications of Diversified Doppler for Random PRI Radar

Shannon D. Blunt, *IEEE Fellow*, Lumumba A. Harnett, *IEEE Member*,  
Brandon Ravenscroft, *IEEE Grad Student Member*, Rachel J. Chang, *IEEE Grad Student Member*,  
Christopher T. Allen, *IEEE Senior Member*, Patrick M. McCormick, *IEEE Member*

**Abstract**—This paper seeks to expand the fundamental understanding of random pulse repetition interval (PRI) staggering radar by formulating a physically meaningful “Doppler manifold” signal model that incorporates slow-time coding and is examined in the context of monostatic, multiple-time-around (MTA) scattering, and multiple-input multiple-output (MIMO) configurations. In so doing, it is found that an intrinsic “range decoherence” effect arises for the MTA and MIMO cases, thereby expanding the means through which separability can be achieved, albeit with rather different degrees of “decoherence amplification”. Moreover, a closed-form solution for the average Doppler response due to random staggering is derived, yielding guidance on the degree necessary to suppress Doppler ambiguities.

**Index Terms**—Doppler processing, PRI staggering, slow-time MIMO, waveform diversity, signal modeling

This work was supported by the Office of Naval Research under Contract #N00014-20-C-1006. DISTRIBUTION STATEMENT A. Approved for public release: distribution unlimited.

**S.D. Blunt** is with the Radar Systems Lab (RSL) and the Electrical Engineering & Computer Science (EECS) Department, University of Kansas, Lawrence, KS 66045 USA (email: [sdblunt@ku.edu](mailto:sdblunt@ku.edu)).

**L.A. Harnett** was with RSL/EECS, University of Kansas. He is now with Leidos, Arlington, VA 22203 USA (email: [Lumumba.A.Harnett@leidos.com](mailto:Lumumba.A.Harnett@leidos.com)).

**B. Ravenscroft** is with RSL/EECS, University of Kansas (email: [g171r597@ku.edu](mailto:g171r597@ku.edu)).

**R.J. Chang** is with RSL/EECS, University of Kansas (email: [rjchang@ku.edu](mailto:rjchang@ku.edu)).

**C.T. Allen** is with RSL/EECS, University of Kansas, (email: [callen@ku.edu](mailto:callen@ku.edu)).

**P.M. McCormick** is with RSL/EECS, University of Kansas (e-mail: [pmccormick@ku.edu](mailto:pmccormick@ku.edu)).

## I. INTRODUCTION

While experimentally demonstrating a practical method for adaptive clutter cancellation and Doppler processing [1] within the context of random PRI staggering [2-7], we came to two realizations that led to the present paper. The first stemmed

from a passage in *Principles of Modern Radar* [8] regarding PRI staggering in general (though in the reference alternatively called “pulse-to-pulse PRF staggering”), which states on page 635:

*“One disadvantage is that the slow-time data sequence in a given range bin is now nonuniformly sampled in slow time, making it more difficult to apply Doppler filtering to the data and greatly complicating analysis. Another is that range-ambiguous mainlobe clutter, if any, can cause large pulse-to-pulse amplitude changes as the PRF varies, since the range of the second-time-around clutter that folds into each range cell will change as the PRF changes. Consequently, pulse-to-pulse PRF stagger is generally used only in low PRF modes in which no range ambiguities are expected.”*

Or simply put, PRI staggering greatly increases signal model complexity, making analysis and processing more difficult. Curiosity aroused, we wished to have a deeper understanding of the mechanisms behind these phenomena, with the hope of establishing a physically meaningful signal model so that future work could potentially address these effects via emerging waveform-diverse capabilities [9] or even exploit them for greater design freedom. As a quick aside for the sake of clarity, note that we are specifically considering pulse-to-pulse staggering within a given coherent processing interval (CPI), as opposed to dwell-to-dwell (or CPI-to-CPI) staggering for which the Chinese Remainder Theorem or Coincidence Algorithm are commonly employed [8,10-12].

The second realization was that slow-time MIMO coding [13-16] (itself a generalization of Doppler-division multiple-access (DDMA) [17,18]) has a connection to PRI staggering. This linkage may possibly be known to some, but we were unable to find where it has previously been discussed in the literature. Indeed, from a phase perspective we show that the combination of slow-time coding (STC) and PRI staggering ultimately leads to the general notion of a “Doppler manifold”, conceptually the same as the more well-known antenna array manifold [19], albeit with phase now dependent on Doppler frequency. This arrangement represents a “complexification” of the receive processing model that we shall refer to as Processing of Diversified Doppler, or PDiD for short, which permits deeper understanding of random PRI staggering and is extensible to MTA and/or MIMO operating modes.

The following rather extensive section examines the PDiD framework for random staggering in three stages. First the Doppler manifold notion is developed for a single emitter (i.e. no MTA or MIMO) to establish the fundamental model structure. This structure is then separately extended into MTA and MIMO scenarios, with a focus on the phenomenological characteristics of each, ultimately leading to general representations that encompass the range “misalignment” (our term) referred to above in [8]. This representation permits sequential realignment according to desired MTA/MIMO components. While not examined here, the MTA and MIMO models are also readily compatible to realize a joint framework having even greater complexity. Due to the extensive nature of this analysis, Appendix A provides a handy reference for the many variables.

Given these respective models, the parameterization trade-space is then investigated to discern the implications of the degree of random staggering. In so doing, analytical Doppler performance first derived in [2] and subsequently upper/lower bounded in [6] is here generalized to obtain a closed-form solution to average Doppler response for random staggering<sup>1</sup> based on the number of pulses in the CPI and limits on a symmetric uniform distribution. Evaluation of this average response suggests nominal values for these limits (an “upward” design pressure) to achieve acceptable suppression of Doppler ambiguities. Conversely, a “downward” design pressure on staggering is observed when MTA or MIMO is incorporated. With that said, it is also shown that far less staggering is required if separability via “range decoherence” is the goal (a concept developed in Sects. II.B and II.C for MTA and MIMO, respectively). It is likewise shown in Sect. III.B.2 that a “decoherence amplification” effect arises (especially for MIMO) and must also be considered.

Finally, a salient aspect of this paper involves addressing the distinction between that which can be precisely modeled and that which cannot. The latter is generally referred to as model discrepancy/inadequacy or structural uncertainty (e.g. [20,21]) and exists within the larger realm of uncertainty quantification in applied mathematics [22]. Due to the very high dynamic range over which radar operates, such effects become particularly important when seeking to develop advanced waveform-diverse modes and associated receive processing because these imperfections lead to multiplicative errors (i.e. not just additive) that can greatly hinder sensitivity. Examples include discretization effects (i.e. straddling), transmitter distortion, and imperfect calibration, all of which can be managed through proper system design, but not eliminated. Accounting for these physically meaningful effects in signal modeling has facilitated the translation of multiple advanced signal processing methods from theory into experimental demonstration (e.g. [1,23-28]), and are addressed where appropriate here as well.

## II. DIVERSIFIED DOPPLER RADAR SIGNAL MODEL

We first describe a fundamental diversified Doppler signal model for monostatic operation that subsumes both PRI staggering and slow-time coding (STC). Based on this model, general processes of in-phase/quadrature (I/Q) sampling, pulse compression, and frequency discretization for Doppler processing are incorporated, while remaining mindful of physical phenomenology and straddling effects. This model is subsequently extended to incorporate MTA scattering and slow-time MIMO, examining the implications of each within the diversified Doppler context.

### A. Monostatic Diversified Doppler at Low PRF

Consider a single pulse-Doppler radar transmitting  $M$  pulses in a dwell, where the  $m$ th PRI  $T_m$  for  $m = 1, 2, \dots, M$  is allowed to vary (or “stagger”) on a pulse-to-pulse basis and the shortest PRI, denoted  $T_{\min} = \min\{T_m\}$ , is long enough that multiple-time-around (MTA) scattering – also known as “range folded” scattering – can be ignored (for now). Each pulse is modulated by the same waveform  $s(t)$ , which has fixed pulse duration  $\tau$  and occupies 3-dB bandwidth  $B$  centered at carrier frequency  $f_c$  after up-conversion (we assume fractional bandwidth  $(B/f_c)$  remains in the narrowband regime [9,29]). The  $m$ th pulse is also modulated by constant phase  $-\pi \leq \theta_m \leq \pi$  via STC [13-18]. The scattering produced by this transmit arrangement and subsequently captured at the radar receiver (subsuming any beamforming) can for the  $m$ th pulse be expressed as

$$y(m, t) = \left[ \sum_{f_D} [s(t; f_D) * x(t; f_D)] e^{j[2\pi f_D T_{\text{acc}}(m) + \theta_m]} + n(m, t) \right] \times \text{rect}[\tau, T_m] \quad (1)$$

for PRI interval  $t \in [0, T_m]$ . Here  $x(t; f_D)$  represents the illuminated range profile of arbitrary scattering having Doppler frequency  $f_D = 2v/\lambda$  in Hz (for radial velocity  $v$  and wavelength  $\lambda$ ),

$$s(t; f_D) = s(t) e^{j2\pi f_D t} \quad \text{for } t \in [0, \tau] \quad (2)$$

is the fast-time Doppler-shifted version of the transmitted waveform (ignoring relativistic effects), the operation  $*$  denotes convolution, and  $n(m, t)$  is thermal noise. The latter is generally represented as white Gaussian with zero-mean and variance (noise power)  $\sigma_n^2$ . The  $\text{rect}[\tau, T_m]$  term in (1) has a unity value between the end of the pulse (at  $\tau$ ) and the end of the  $m$ th PRI (when the next pulse would begin transmission) and zero otherwise, thereby representing the observation interval as delimited by the transmit-receive (T-R) switch used in most pulsed radars. The value  $T_{\text{acc}}(m)$  in the exponent of (1) is the accumulated slow-time at the beginning of the  $m$ th PRI, which is

<sup>1</sup> It was claimed in [2] that a closed-form solution in this context is impossible but is realized here by reformulating the analytical problem to be symmetric.

$$T_{\text{acc}}(m) = \sum_{q=0}^{m-1} T_q \quad (3)$$

for  $m = 1, 2, \dots, M$ , with initial condition  $T_0 = 0$  and thus  $T_{\text{acc}}(1) = 0$  for the first pulse.

For diverse PRIs, it is useful to express the average PRI

$$T_{\text{avg}} = \frac{1}{M} \sum_{m=1}^M T_m \quad (4)$$

so that the  $m$ th PRI for  $m = 1, 2, \dots, M$  (i.e. not for  $m = 0$ ) can be defined as

$$T_m = T_{\text{avg}} + \Delta T_m. \quad (5)$$

Thus  $\Delta T_0 = T_0 = 0$  and all other  $\Delta T_m$  are independently drawn from some fixed interval  $[-\delta, +\delta]$ . Based on (4) and (5), clearly  $\sum_{m=1}^M (\Delta T_m) = 0$  and the temporal extent of the CPI remains fixed regardless of the staggering sequence for a given  $T_{\text{avg}}$ . Per (5), it is also useful to express each PRI for  $m = 1, 2, \dots, M$  in terms of the normalized value

$$\varepsilon_m = \frac{T_m}{T_{\text{avg}}} = 1 + \Delta \varepsilon_m, \quad (6)$$

where  $\Delta \varepsilon_m = \Delta T_m / T_{\text{avg}}$  (and  $\varepsilon_0 = \Delta \varepsilon_0 = 0$ ). Therefore  $-\bar{\delta} \leq \Delta \varepsilon_m \leq +\bar{\delta}$ , for  $\bar{\delta} = \delta / T_{\text{avg}}$  being the normalized stagger limit in percentage form (discussed further in Sect. III).

The accumulated time in (3), for  $m \geq 2$ , can then also be written as the normalized value

$$\begin{aligned} \varepsilon_{\text{acc}}(m) &= \frac{T_{\text{acc}}(m)}{T_{\text{avg}}} = \sum_{q=0}^{m-1} \varepsilon_q \\ &= (m-1) + \sum_{q=1}^{m-1} \Delta \varepsilon_q \\ &= (m-1) + \Delta \varepsilon_{\text{acc}}(m), \end{aligned} \quad (7)$$

where  $\Delta \varepsilon_{\text{acc}}(1) = \varepsilon_{\text{acc}}(1) = \varepsilon_0 = 0$  for the first pulse and  $\Delta \varepsilon_{\text{acc}}(m)$  represents the normalized deviation from a uniform PRI accumulated over the  $(m-1)$  previous PRIs. Thus the constant CPI length also means  $\sum_{m=1}^M (\Delta \varepsilon_m) = [\Delta \varepsilon_{\text{acc}}(M) + \Delta \varepsilon_M] = 0$  via (6) and (7); i.e. staggering deviation is conserved for fixed CPI extent.

Using (4), normalized Doppler (nD) frequency can likewise be expressed as

$$f_{\text{nD}} = f_D T_{\text{avg}} \quad (8)$$

so that part of the exponential in (1) can now be rewritten as

$$f_D T_{\text{acc}}(m) = \left( f_D T_{\text{avg}} \right) \frac{T_{\text{acc}}(m)}{T_{\text{avg}}} = f_{\text{nD}} \varepsilon_{\text{acc}}(m), \quad (9)$$

in which the  $\varepsilon_{\text{acc}}(m)$  term serves as a linear ‘‘Doppler-to-phase slope’’ in the exponential.

We can thus pose (1) via normalized values from (9) as

$$y(m, t) = \left[ \sum_{f_D} [s(t; f_D) * x(t; f_D)] e^{j[2\pi f_{\text{nD}} \varepsilon_{\text{acc}}(m) + \theta_m]} + n(m, t) \right] \times \text{rect}[\tau, T_m] \quad (10)$$

to facilitate construction of the  $M \times 1$  normalized Doppler steering vector

$$\begin{aligned} \mathbf{v}(f_{\text{nD}}) &= \left[ e^{j\theta_1} e^{j[2\pi f_{\text{nD}} \varepsilon_{\text{acc}}(2) + \theta_2]} \dots e^{j[2\pi f_{\text{nD}} \varepsilon_{\text{acc}}(M) + \theta_M]} \right]^T \\ &= \bar{\mathbf{v}}(f_{\text{nD}}) \odot \mathbf{d}(f_{\text{nD}}; \Delta \boldsymbol{\varepsilon}_{\text{acc}}, \boldsymbol{\theta}) \end{aligned} \quad (11)$$

with  $\odot$  denoting Hadamard product. Using the decomposition  $\varepsilon_{\text{acc}}(m) = (m-1) + \Delta \varepsilon_{\text{acc}}(m)$  from (7), the component vectors in (11) can be expressed as the usual Vandermonde form

$$\bar{\mathbf{v}}(f_{\text{nD}}) = \left[ 1 \quad e^{j2\pi(1)f_{\text{nD}}} \quad \dots \quad e^{j2\pi(M-1)f_{\text{nD}}} \right]^T \quad (12)$$

having linear phase progression due to uniform PRI, and a phase deviation vector

$$\begin{aligned} \mathbf{d}(f_{\text{nD}}; \Delta \boldsymbol{\varepsilon}_{\text{acc}}, \boldsymbol{\theta}) &= \left[ e^{j\theta_1} e^{j[2\pi f_{\text{nD}} \Delta \varepsilon_{\text{acc}}(2) + \theta_2]} \right. \\ &\quad \left. \dots e^{j[2\pi f_{\text{nD}} \Delta \varepsilon_{\text{acc}}(M) + \theta_M]} \right]^T, \end{aligned} \quad (13)$$

where  $\Delta \boldsymbol{\varepsilon}_{\text{acc}} = [0 \quad \Delta \varepsilon_{\text{acc}}(2) \dots \Delta \varepsilon_{\text{acc}}(M)]^T$  captures the phase slope deflections caused by staggering and  $\boldsymbol{\theta} = [\theta_1 \quad \theta_2 \dots \theta_M]^T$  collects the slow-time phase coding.

Now consider a high-level perspective on what the above structure means. In the same way that an array manifold [19] is parameterized by the physical attributes/locations of the elements in a phased array while being functionally dependent on spatial angle, we can view (11) as a ‘‘Doppler manifold’’ parameterized by the set of  $T_m$  and  $\theta_m$  values and functionally dependent on Doppler frequency. Consequently, we can think of deviations relative to the uniform PRI model of (12) as applying different ‘‘affine Doppler transformations’’ based on the combination of *i*) STC via  $\theta_m$  that redefines steering vector structure for zero-Doppler, where clutter generally resides, and *ii*) Doppler-to-phase slope deflections via  $\Delta \varepsilon_{\text{acc}}(m)$ , which can extend unambiguous Doppler and/or introduce decoherence of MTA/MIMO components (described in Sect. III.B). In other words, this two-fold manner of diversification expands the ways in which different responses can be separated in the Doppler domain.

When no staggering occurs,  $T_m = T_{\text{avg}}$ , each  $\varepsilon_m = 1$ , and  $\Delta \varepsilon_{\text{acc}}(m) = 0$  for all  $m$ , so (13) becomes

$$\mathbf{d}(f_{\text{nD}}; \Delta \boldsymbol{\varepsilon}_{\text{acc}} = 0, \boldsymbol{\theta}) = \left[ e^{j\theta_1} \quad e^{j\theta_2} \quad \dots \quad e^{j\theta_M} \right]^T \quad (14)$$

and (11) reverts to the slow-time coded, uniform PRI steering vector

$$\mathbf{v}(f_{\text{nD}}) = \left[ e^{j\theta_1} e^{j[2\pi(1)f_{\text{nD}} + \theta_2]} \quad \dots \quad e^{j[2\pi(M-1)f_{\text{nD}} + \theta_M]} \right]^T. \quad (15)$$

This form, which simplifies to (12) when  $\theta_1 = \dots = \theta_M = 0$ , changes the zero-Doppler response within the Doppler manifold, yet retains the unambiguous Doppler extent of (12). Specifically, without PRI staggering any value of  $|f_{\text{nd}}| > 0.5$  is aliased back into the  $[-0.5, +0.5]$  unambiguous normalized Doppler interval, the limits of which correspond to the unnormalized interval  $[-\text{PRF}/2, +\text{PRF}/2]$ , for  $\text{PRF} = 1/T_{\text{avg}}$  in the uniform case.

It is well known (see [8] Chap. 17) that PRI staggering extends the  $[-0.5, +0.5]$  unambiguous normalized Doppler space, which can be expressed as  $f_{\text{nd}} \in \pm 0.5\beta$  for

$$\beta = T_{\text{avg}} \times \text{LCM}\{f_1, f_2, \dots, f_M\}, \quad (16)$$

with  $\text{LCM}\{\bullet\}$  denoting the *least common multiple* of the arguments and  $f_m = 1/T_m$ . For uniform PRI, the value of (16) is  $\beta = T_{\text{avg}}(1/T_{\text{avg}}) = 1$ , while PRI staggering yields  $\beta > 1$ . Of course, the trade-off for expanding unambiguous Doppler in this manner, unlike the attendant reduction in unambiguous range otherwise obtained for uniform PRI, is a tendency toward a flattened Doppler sidelobe pedestal (later illustrated in Figs. 10-14). One can view this trade-off as a ‘‘conservation of ambiguity’’ [9] in which a flatter sidelobe floor inversely proportional to  $M$  is realized in exchange for avoiding a repeated mainlobe. Moreover, while (16) suggests an ‘‘all or nothing’’ outcome for Doppler ambiguities, we shall see that the reduction of ambiguity peaks is really more a gradual effect until a nominal degree of staggering is achieved (e.g. consider the LCM produced by small, yet irrational, stagger deviations).

Pulse compression can be performed on the received signal model of (10) to obtain

$$\begin{aligned} z(m, t) &= h(t) * y(m, t) \\ &\approx \sum_{f_{\text{D}}} [h(t) * s(t; f_{\text{D}}) * x(t; f_{\text{D}})] e^{j[2\pi f_{\text{nd}} \varepsilon_{\text{acc}}(m) + \theta_m]} \\ &\quad + h(t) * n(m, t) \\ &\approx \sum_{f_{\text{D}}} [r(t; f_{\text{D}}) * x(t; f_{\text{D}})] e^{j[2\pi f_{\text{nd}} \varepsilon_{\text{acc}}(m) + \theta_m]} \\ &\quad + \tilde{n}(m, t) \\ &\approx \sum_{f_{\text{D}}} [\tilde{x}(t; f_{\text{D}})] e^{j[2\pi f_{\text{nd}} \varepsilon_{\text{acc}}(m) + \theta_m]} + \tilde{n}(m, t), \end{aligned} \quad (17)$$

where  $h(t)$  is a matched/mismatched filter for waveform  $s(t)$  [9,30], with  $r(t; f_{\text{D}}) = h(t) * s(t; f_{\text{D}})$  the subsequent filter response (including any fast-time Doppler mismatch). Consequently,  $\tilde{x}(t; f_{\text{D}}) = r(t; f_{\text{D}}) * x(t; f_{\text{D}})$  is a version of the illuminated scattering that is shaped by pulse compression, realizing coherent integration gain according to the waveform’s time-bandwidth product ( $\tau B$ ) when  $f_{\text{D}}$  is sufficiently small and otherwise accounting for mismatch loss according to the waveform’s Doppler tolerance.

The use of  $\approx$  in (17) is due to pulse eclipsing effects [31] at the edges of the observation interval arising from the  $\text{rect}[\tau, T_m]$  term in (1) and (10) caused by T-R switching. Pulse eclipsing yields a partial matched/mismatched filter response

via  $h(t) * \bar{s}(t; f_{\text{D}}) * x(t; f_{\text{D}})$ , where  $\bar{s}(t; f_{\text{D}})$  is a truncated version of the waveform in (2) depending on proximity to the edges of the observation interval. Thus, the degree of pulse compression gain and associated sidelobe structure change near the edges of the observation interval. While this nonstationary (yet deterministic) range effect is generally not a major concern as long as the radar duty cycle is modest, it adds another complicating factor to MTA/MIMO scattering, particularly in the context of PRI staggering.

Since radar pulses have finite time support, it is technically not possible to perform Nyquist sampling since bandlimiting is not achieved, though a well-designed RF system can realize good enough spectral containment that the effect is negligible if sufficient over-sampling relative to 3-dB bandwidth is employed (i.e. capture spectral roll-off). A somewhat related effect is range straddling [32,33], which introduces error because physical scattering is a continuum, meaning there is an inherent limit to the fidelity of any discretized receive model. Of course, fidelity is still improved through greater over-sampling, albeit to the degree permitted by throughput limits on signal dimensionality and computational cost. Bearing this fidelity versus dimensionality trade-space in mind, receive I/Q sampling can be performed in which the discretized responses from  $M$  pulses at the  $\ell$ th range sample can collectively be written as

$$\begin{aligned} \mathbf{z}(\ell) &= \sum_{f_{\text{D}}} \tilde{\mathbf{x}}(\ell; f_{\text{D}}) \mathbf{v}(f_{\text{nd}}) + \tilde{\mathbf{n}}(\ell) \\ &\approx \mathbf{V} \tilde{\mathbf{x}}(\ell) + \tilde{\mathbf{n}}(\ell), \end{aligned} \quad (18)$$

where the second line involves discretization in Doppler as well (thereby incurring further straddling error). Here  $\tilde{\mathbf{n}}(\ell)$  is the  $M \times 1$  vector of sampled noise after pulse compression, while the columns of  $M \times N$  matrix  $\mathbf{V}$  contain versions of the normalized Doppler steering vector of (11) according to a discretization of  $f_{\text{nd}}$  at some specified granularity and over a Doppler interval for which illuminated radial velocities are physically meaningful. Finally, the  $N \times 1$  vector  $\tilde{\mathbf{x}}(\ell)$  contains scattering values (after I/Q sampling and pulse compression) for the  $\ell$ th range cell that are discretized across Doppler in the same manner as the steering vectors in  $\mathbf{V}$ .

For uniform PRI, the Doppler mainlobe peak and first null are separated by a normalized Doppler of  $1/M$ , such that  $N = M$  steering vectors offset by  $1/M$  span the unambiguous interval  $[-0.5, +0.5]$ . However, like I/Q sampling in time, this discretized Doppler representation means that some degree of Doppler straddling ([8] Chap. 14) is unavoidable since  $f_{\text{D}}$ , and thus  $f_{\text{nd}}$ , also lies on a continuum. Consequently, over-sampling the Doppler spectrum by factor  $K$  likewise achieves a higher fidelity representation (to reduce Doppler straddling at the cost of higher dimensionality), thus realizing  $N = KM$  and normalized Doppler discretized with a granularity of  $1/N = 1/MK$ .

For the same factor  $K$ , it follows from (16) that a given arrangement of PRI staggering corresponds to the extension

$N = \lceil \beta KM \rceil$ , for  $\beta \geq 1$  and  $\lceil \bullet \rceil$  the ceiling operation, thereby representing the extended unambiguous normalized Doppler space at the same granularity. Since (16) could conceivably be far higher than is physically meaningful (e.g. via irrational staggers), a judicious choice is to replace  $\beta$  with some reasonable value  $\beta_{\text{mov}}$  that sufficiently captures the radial velocities of realistic movers. Thus, the number of columns in  $\mathbf{V}$  becomes  $N = \lceil \beta_{\text{mov}} KM \rceil$ , where  $\beta \geq \beta_{\text{mov}} \geq 1$ .

In general, standard Doppler processing (DP) can be applied to (18) by performing

$$\begin{aligned} \hat{\mathbf{x}}_{\text{DP}}(\ell) &= \mathbf{W}_{\text{DP}}^H \mathbf{z}(\ell) \\ &\cong \mathbf{W}_{\text{DP}}^H \mathbf{V} \tilde{\mathbf{x}}(\ell) + \mathbf{W}_{\text{DP}}^H \tilde{\mathbf{n}}(\ell), \end{aligned} \quad (19)$$

where  $(\bullet)^H$  denotes the complex-conjugate transpose (or Hermitian) operation, the  $M \times N$  matrix  $\mathbf{W}_{\text{DP}} = \mathbf{V}$ , and  $\hat{\mathbf{x}}_{\text{DP}}(\ell)$  is the resulting estimated response across the unambiguous Doppler interval of interest, again noting that discretized Doppler necessarily introduces some degree of straddling error (second line of (19)). An additional signal gain of  $M$  is obtained relative to noise due to coherent matching of like columns in  $\mathbf{V}$ , with an associated Doppler mainlobe roll-off due to high correlation between nearby columns in  $\mathbf{V}$  arising from over-sampling (by  $K$ ) to reduce Doppler straddling effects. Thus, a given row or column of the resulting  $N \times N$  Hermitian matrix  $(\mathbf{V}^H \mathbf{V})$  exemplifies the Doppler mainlobe and sidelobes for steering vector  $\mathbf{v}(f_{\text{nD}})$  from (11) for the particular staggering arrangement (including the uniform case). It was recently experimentally shown in [1] that (19) can be readily extended to incorporate clutter cancellation.

The Doppler response at some normalized frequency  $f_{\text{nD},1}$  resulting from scattering at  $f_{\text{nD},2}$  is clearly identical to the Doppler response one would obtain at difference  $(f_{\text{nD},2} - f_{\text{nD},1})$  resulting from scattering at  $f_{\text{nD}} = 0$ . This shift invariance means we can generalize the assessment of a given staggering sequence by defining the zero-referenced Doppler response

$$\begin{aligned} u(f_{\text{nD}}) &= \mathbf{v}^H(f_{\text{nD}}) \mathbf{v}(f_{\text{nD}} = 0) \\ &= \sum_{m=1}^M e^{-j[2\pi f_{\text{nD}} \varepsilon_{\text{acc}}(m) + \theta_m]} e^{j\theta_m} = \sum_{m=1}^M e^{-j2\pi f_{\text{nD}} \varepsilon_{\text{acc}}(m)} \quad (20) \\ &= \sum_{m=1}^M e^{-j2\pi (m-1) f_{\text{nD}}} e^{-j2\pi f_{\text{nD}} \Delta \varepsilon_{\text{acc}}(m)} \end{aligned}$$

in which the STC terms in  $\mathbf{v}(f_{\text{nD}} = 0) = [e^{j\theta_1} \ e^{j\theta_2} \ \dots \ e^{j\theta_M}]^T$  via (11) are cancelled and the last line illustrates decomposition into uniform and deflection components according to (7). In other words, staggering produces a perturbation of the usual sum of phase terms, which is explored further in Sect. III. For uniform PRIs, the magnitude of (20) becomes a Dirichlet kernel (periodic sinc function).

An integrated Doppler sidelobe level (IDSL) metric can be quantified using (20) as

$$\text{IDSL} = \frac{\int_{f_{\text{nD}}=1/M}^{0.5} |u(f)|^2 df}{\int_{f_{\text{nD}}=0}^{1/M} |u(f)|^2 df}, \quad (21)$$

where the interval  $[0, 1/M]$  in the denominator captures the zero-Doppler mainlobe peak out to the first Doppler null (per uniform PRI case), the remaining  $[1/M, 0.5]$  interval in the numerator captures a fixed portion of the Doppler sidelobes, and we have invoked symmetry for  $\pm f_{\text{nD}}$ . The fixed-interval perspective in (21) provides a direct way to compare the sidelobe impact of different staggering arrangements within the fundamental unambiguous Doppler interval established by a uniform CPI of  $M$  pulses.

Since PRI staggering extends the unambiguous Doppler interval through diversification of Doppler manifold phase slopes, it is also useful to specify an extended Doppler sidelobe level (EDSL) metric over the entire unambiguous normalized Doppler interval, which is specific to a particular staggering arrangement. This metric can take the form

$$\text{EDSL} = \frac{\int_{f_{\text{nD}}=1/M}^{0.5\beta} |u(f)|^2 df}{\beta \int_{f_{\text{nD}}=0}^{1/M} |u(f)|^2 df}, \quad (22)$$

where the sidelobe interval in the numerator of (21) has now been extended from 0.5 to  $0.5\beta$  via (16) and the denominator is the same as (21) except for the inclusion of normalization by  $\beta (\geq 1)$  to account for interval extension. As noted before (19), it may be more meaningful to set  $\beta \rightarrow \beta_{\text{mov}}$  in (22) so that only radial velocities of realistic movers are included.

For example, Fig. 1 shows the Doppler response of (20) for  $M = 50$  pulses using both uniform PRIs and randomly staggered PRIs with  $\bar{\delta} = 35\%$ , with the latter depicting the maximum and mean values versus Doppler evaluated over 1000 independent stagger trials. The vertical dashed lines indicate different values for  $\beta$ , and are also included on the uniform PRI plot as reference. Specifically, consider the EDSL plot vs.  $\beta$  depicted in Fig. 2, where we have also applied (22) to the uniform Doppler response, which obviously repeats. The reason for doing so is because Fig. 2 reveals that, for all practical purposes, integrated Doppler ambiguity is essentially conserved as one extends to higher values of  $\beta$  because the maximum, minimum, and mean traces for staggering (over the 1000 trials) closely follow the EDSL evaluation of the uniform response where repetitions of the mainlobe occur. Of course, the benefit of staggering arises from the sidelobe flattening observed in Fig. 1, which facilitates improved discrimination of movers at higher Doppler.

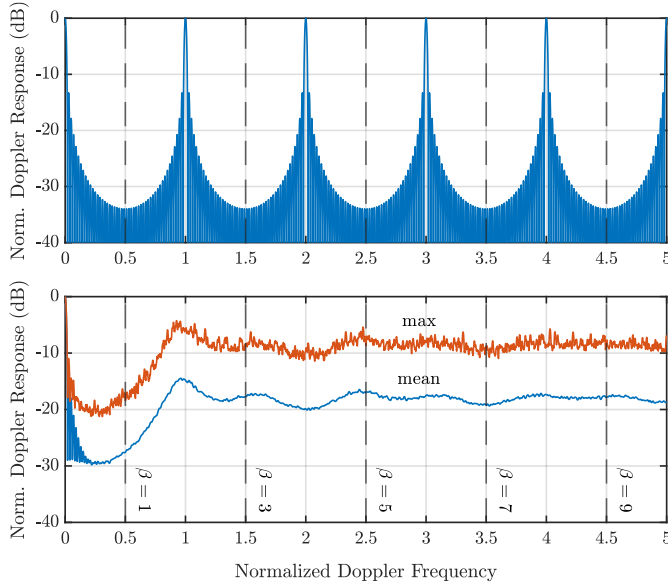


**Fig. 1.** Normalized Doppler response for  $M = 50$  pulses with (top) uniform PRIs and (bottom) random staggers uniformly distributed within  $\pm 35\%$ , showing the maximum and mean over 1000 independent trials

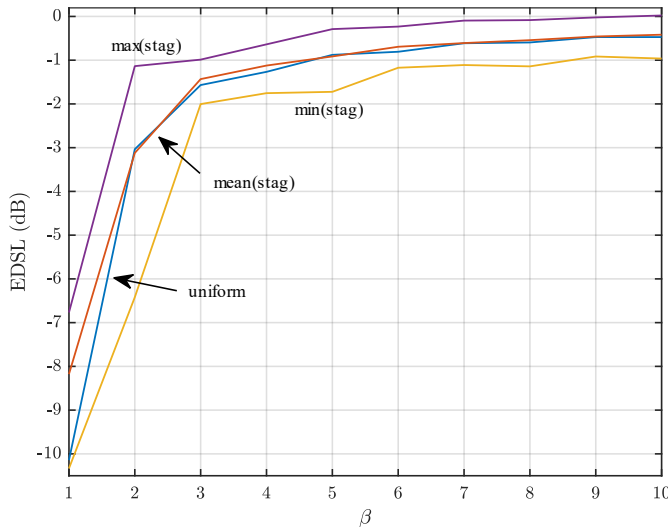


**Fig. 2.** Evaluation of EDSL metric from (22) vs.  $\beta$  for  $M = 50$  pulses, comparing uniform PRI with the mean, maximum, and minimum EDSL values across 1000 independent trials for random staggers within  $\pm 35\%$

### B. PDiD Implications for MTA Scattering

Since it is known that STC can be used to discriminate between multiple-time-around (MTA) – or “range folded” – scattering [34–37], now consider an extension to the PDiD model that accounts for multiple range ambiguities. Denoting  $G$  as the number of observable range intervals (with  $G = 1$  simplifying to the previous case), then  $(G - 1)$  “fill pulses” ([8] Chap. 17) are needed so that each PRI contains scattering from all  $G$  intervals. For convenience denote the  $G$ th pulse as the beginning of the CPI, so that indices  $m = 1, \dots, (G - 1)$  correspond to preceding fill pulses, followed by CPI pulse indices  $m = G, \dots, (M + G - 1)$ . Likewise index the  $G$  range ambiguities as  $g = 1, \dots, G$ , with  $g = 1$  denoting the first (i.e.

closest) range interval and  $g = G$  the farthest. For reference, Fig. 3 illustrates the  $G = 3$  pulse arrangement for uniform PRI, where red blocks indicate fill pulses, blue blocks are the  $M$  pulses in the CPI, and gray regions are observation intervals.

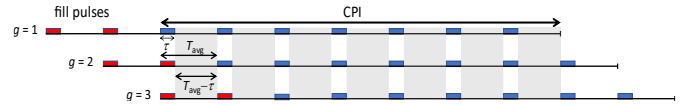


**Fig. 3.** Pulse arrangement for uniform PRI and  $G = 3$  range ambiguities, with fill pulses in red, the  $M$  pulses of the CPI in blue, and gray regions the observation (or listen) intervals.

For pulse indices  $m = G, \dots, (M + G - 1)$  in the CPI, and noting PRI staggering introduces shuffling of MTA scattering, the received model of (10) can be generalized as

$$y(m, t) = \left( \sum_{f_D} [s(t; f_D) * x(t; f_D)] e^{j[2\pi f_{nD} \varepsilon_{acc}(m) + \theta_m]} + n(m, t) \right. \\ \left. + \sum_{g=2}^G \sum_{f_D} \left[ s(t; f_D) * x\left(t + \sum_{\tilde{g}=1}^{g-1} T_{m-\tilde{g}}; f_D\right) \right] e^{j[2\pi f_{nD} \varepsilon_{acc}(m-g+1) + \theta_{m-g+1}]} \right) \\ \times \text{rect}[\tau, T_m], \quad (23)$$

where the first line is identical to (10), corresponding to the first range interval ( $g = 1$ ), and the summation in the second line captures the remaining  $(G - 1)$  MTA intervals. Because fast-time  $t$  (and therefore range) is referenced to the first interval for the  $m$ th PRI, each subsequent MTA interval involves an accumulated time offset to account for it being referenced to a previous PRI. The exponential phase component for each MTA interval is likewise referenced to a prior accumulated time (normalized) and STC value for a previous PRI.

Using the exponential phase terms in (23), we can similarly generalize (11)–(13) to define an  $M \times 1$  normalized Doppler steering vector for each of the  $g = 1, \dots, G$  range intervals as

$$\mathbf{v}_g(f_{nD}) = \left[ e^{j[2\pi f_{nD} \varepsilon_{acc}(\tilde{G}+1) + \theta_{\tilde{G}+1}]} \quad e^{j[2\pi f_{nD} \varepsilon_{acc}(\tilde{G}+2) + \theta_{\tilde{G}+2}]} \right. \\ \left. \dots \quad e^{j[2\pi f_{nD} \varepsilon_{acc}(\tilde{G}+M) + \theta_{\tilde{G}+M}]} \right]^T \\ = \bar{\mathbf{v}}(f_{nD}) \odot \mathbf{d}(f_{nD}; \Delta \varepsilon_{acc, \tilde{G}}, \boldsymbol{\theta}_{\tilde{G}}), \quad (24)$$

using  $\tilde{G} = G - g$  to simplify notation, with normalized offsets  $\Delta \varepsilon_{acc, \tilde{G}} = [\Delta \varepsilon_{acc}(\tilde{G}+1) \quad \Delta \varepsilon_{acc}(\tilde{G}+2) \quad \dots \quad \Delta \varepsilon_{acc}(\tilde{G}+M)]^T$  and coding  $\boldsymbol{\theta}_{\tilde{G}} = [\theta_{\tilde{G}+1} \quad \theta_{\tilde{G}+2} \quad \dots \quad \theta_{\tilde{G}+M}]^T$ . For  $g = G$  (so  $\tilde{G} = 0$ ), we again have  $\Delta \varepsilon_{acc}(\tilde{G}+1) = \Delta \varepsilon_{acc}(1) = 0$ . As  $g$  increases, the elements in the corresponding steering vector of (24) shift downward, with new terms associated with fill pulses (and their particular phase dependence on staggering/STC) inserted at the top. Consequently, because each element possesses a distinct STC phase and Doppler-to-phase slope, the diversified Doppler manifold characterized by each range interval’s steering vector is likewise distinct.

Performing pulse compression on (23) then leads to

$$\begin{aligned}
z(m, t) &= h(t) * y(m, t) \\
&\approx \sum_{f_D} [\tilde{x}(t; f_D)] e^{j[2\pi f_{nD} \epsilon_{acc}(m) + \theta_m]} + \tilde{n}(m, t) \\
&\quad + \sum_{g=2}^G \sum_{f_D} \tilde{x}_{m,g}(t, f_D) e^{j[2\pi f_{nD} \epsilon_{acc}(m-g+1) + \theta_{m-g+1}]} \quad (25) \\
&\approx \tilde{\psi}_1(m, t) + \tilde{n}_1(m, t) + \sum_{g=2}^G \tilde{\psi}_{g,1}(m, t),
\end{aligned}$$

for  $\tilde{x}(t; f_D)$  once again a version of scattering shaped by the illuminated waveform and subsequent pulse compression filtering, while  $\tilde{x}_{m,g}(t, f_D) = \tilde{x}(t + \sum_{\bar{g}=1}^{g-1} T_{m-\bar{g}}; f_D)$  for  $g > 1$  is pulse compressed MTA scattering that is delay-shifted differently in each PRI due to staggering. On the last line of (25) we have denoted  $\tilde{\psi}_1(m, t)$  as the term corresponding to the first interval (subsuming the complete staggering/STC phase component), which is identical to that in (17). We have likewise denoted the  $g$ th MTA interval response (for each  $g \neq 1$ ) as  $\tilde{\psi}_{g,1}(m, t)$  since it is organized relative to the 1<sup>st</sup> range interval. Further, the pulse compressed noise has been relabeled as  $\tilde{n}_1(m, t)$  for consistency with further development below. As discussed in Sect. II.A, pulse eclipsing imposed by T-R switching via the  $\text{rect}[\tau, T_m]$  term in (23) necessitates the use of  $\approx$  in both lines of (25) and also introduces a blind-range dependence on the particular stagger sequence for each MTA interval.

By itself, the  $\tilde{\psi}_1(m, t)$  term in (25) would realize the vectorized form in (18) after performing I/Q sampling and Doppler discretization because coherent scattering for the first interval is already range-aligned across the CPI. In contrast, the inherent staggering offsets relative to the 1<sup>st</sup> range interval causes the  $\tilde{\psi}_{g,1}(m, t)$  components in (25) to not be range-aligned across the CPI, resulting in decoherence that hinders cancellation of MTA clutter (as noted in [8]).

In principle, however, the responses for the  $g \geq 2$  intervals could be “re-cohered” by performing per-PRI range realignment on (25) in a manner that compensates for accumulated stagger offsets. Specifically, recalling  $T_m = T_{avg} + \Delta T_m$  from (5), and henceforth denoting the overall response in (25) as  $z(m, t) \rightarrow z_1(m, t)$  for consistency, the  $m$ th PRI from (25) could alternatively be range realigned according to the  $g = 2$  MTA interval via

$$\begin{aligned}
z_2(m, t) &= z(m, t - \Delta T_{m-1}) \\
&\approx \sum_{f_D} [\tilde{x}(t + T_{avg}; f_D)] e^{j[2\pi f_{nD} \epsilon_{acc}(m-1) + \theta_{m-1}]} \\
&\quad + \tilde{n}(m, t - \Delta T_{m-1}) + \sum_{f_D} \tilde{x}_{m,1}(t; f_D) e^{j[2\pi f_{nD} \epsilon_{acc}(m) + \theta_m]} \quad (26) \\
&\quad + \sum_{g=3}^G \sum_{f_D} \tilde{x}_{m,g}(t; f_D) e^{j[2\pi f_{nD} \epsilon_{acc}(m-g+1) + \theta_{m-g+1}]} \\
&\approx \tilde{\psi}_2(m, t) + \tilde{n}_2(m, t) + \sum_{\substack{g=1 \\ g \neq 2}}^G \tilde{\psi}_{g,2}(m, t),
\end{aligned}$$

with  $\tilde{\psi}_2(m, t)$  now the range-aligned response according to the 2<sup>nd</sup> interval and  $\tilde{n}_2(m, t)$  the corresponding pulse compressed noise after range realignment. Here  $\tilde{\psi}_{g,2}(m, t)$  in the last line is comprised of pulse compressed scattering  $\tilde{x}_{m,1}(t, f_D) = \tilde{x}(t - \Delta T_{m-1}; f_D)$  from range interval  $g = 1$  plus  $\tilde{x}_{m,g}(t, f_D) = \tilde{x}(t - \Delta T_{m-1} + \sum_{\bar{g}=1}^{g-1} T_{m-\bar{g}}; f_D)$  for  $g = 3, \dots, G$ , the collection of which has been organized relative to the 2<sup>nd</sup> range interval and is therefore decohered. We can generalize (26) for range alignment to the  $\bar{g}$ th MTA interval as

$$\begin{aligned}
z_{\bar{g}}(m, t) &= z(m, t - \sum_{\bar{g}=1}^{\bar{g}-1} \Delta T_{m-\bar{g}}) \\
&\approx \tilde{\psi}_{\bar{g}}(m, t) + \tilde{n}_{\bar{g}}(m, t) + \sum_{\substack{g=1 \\ g \neq \bar{g}}}^G \tilde{\psi}_{g,\bar{g}}(m, t) \quad (27)
\end{aligned}$$

where  $\tilde{\psi}_{\bar{g}}(m, t)$ , like in (26), is coherently aligned to scattering  $\tilde{x}(t + (\bar{g}-1)T_{avg}; f_D)$  and the other  $(G-1)$  intervals denoted as  $\tilde{\psi}_{g,\bar{g}}(m, t)$  for  $g \neq \bar{g}$  are not range-aligned.

Using (25)-(27), we can now leverage (18) to write an associated I/Q sampled and Doppler discretized version that is range-aligned according to the  $\bar{g}$ th interval as

$$\begin{aligned}
\mathbf{z}_{\bar{g}}(\ell) &= \sum_{f_D} \tilde{x}_{\bar{g}}(\ell; f_D) \mathbf{v}_{\bar{g}}(f_{nD}) \\
&\quad + \sum_{\substack{g=1 \\ g \neq \bar{g}}}^G \sum_{f_D} [\tilde{\mathbf{x}}_g(\ell; f_D) \odot \mathbf{v}_g(f_{nD})] + \tilde{\mathbf{n}}_{\bar{g}}(\ell) \quad (28) \\
&\approx \mathbf{V}_{\bar{g}} \tilde{\mathbf{x}}_{\bar{g}}(\ell) + \sum_{\substack{g=1 \\ g \neq \bar{g}}}^G [\tilde{\mathbf{X}}_g(\ell) \odot \mathbf{V}_g] \mathbf{1}_{N \times 1} + \tilde{\mathbf{n}}_{\bar{g}}(\ell),
\end{aligned}$$

where the Doppler-discretized  $\mathbf{V}_{\bar{g}} \tilde{\mathbf{x}}_{\bar{g}}(\ell)$  term is the same as in (18), albeit for the  $\bar{g}$ th interval and subsuming the  $(\bar{g}-1)T_{avg}$  delay offset, with  $\tilde{\mathbf{n}}_{\bar{g}}(\ell)$  the collection of  $M$  noise samples after range realignment for the  $\bar{g}$ th interval. The term  $[\tilde{\mathbf{X}}_g(\ell) \odot \mathbf{V}_g] \mathbf{1}_{N \times 1}$  in (28) involves collecting the misaligned scattering for the  $g \neq \bar{g}$  range interval and each discretized

Doppler across the  $M$  PRIs into  $M \times N$  matrix  $\tilde{\mathbf{X}}_g(\ell)$ , Hadamard multiplying with the corresponding  $M \times N$  discretized Doppler matrix  $\mathbf{V}_g$  (diversified according to the particular staggering/STC), and then multiplying the result by the all-one vector  $\mathbf{1}_{N \times 1}$  to sum these incoherent components across Doppler. A noteworthy observation from (28) is that misaligned scattering from the  $g \neq \bar{g}$  range intervals would be perceived as uncorrelated noise in slow-time, yet still retain the spatial dependence of transmit/receive beamforming.

There are some caveats to this range realignment process. Clearly, any realignment by a subsample shift would be performed in the frequency domain. There is also the implicit assumption that the complete range interval for  $z(m, t - \sum_{\bar{g}=1}^{\bar{g}-1} \Delta T_{m-\bar{g}})$  in (27) exists across all  $M$  PRIs, which is not true for portions near the edges due to T/R switching. Moreover, fast-time nonstationarity of matched/mismatched filter responses near PRI edges due to pulse eclipsing (per Sect. II.A) imposes slow-time nonstationarity when range realignment is performed, thereby inhibiting fidelity in these regions. Taken together, these effects further restrict the meaningful extent of MTA range observation intervals due to expanded blind ranges, suggesting the need for more detailed modeling in these regions to enable development of receive processing akin to pulse blanking compensation (e.g. [38]) performed on a range-dependent basis for each MTA interval. Indeed, [39] discusses various methods of slow-time interpolation to contend with this effect specific to synthetic aperture radar (SAR).

Bearing these limitations in mind, we can encapsulate the above discussion by defining the operator  $\Gamma_{\bar{g}}\{\bullet\}$  that performs range realignment across the  $M$  PRIs of (27) such that the specific signal structure in (28) is obtained via

$$\mathbf{z}_{\bar{g}}(\ell) = \Gamma_{\bar{g}}\{\mathbf{z}_{\dot{g}}(\ell)\} \quad (29)$$

for  $\dot{g} \neq \bar{g}$ , where  $\dot{g}$  denotes prior alignment according to some other arbitrary range interval. Consequently, (29) facilitates sequentially changing between different alignments, where one could employ appropriate receive processing at each step (e.g. cancelling clutter within the given range interval). Indeed, from a moving target indication (MTI) standpoint it stands to reason that one could step through each of the  $G$  intervals performing clutter cancellation, and then subsequently repeat the realignment sequence to estimate movers in each range interval (within the meaningful range extent determined by edge effects).

Per (28), we also observe that only one Doppler manifold can be coherent across the CPI for each particular range alignment. It follows that a seemingly straightforward assessment of separability of MTA intervals based on different values of  $g$ , which one might conceivably perform via the inner product of steering vectors from (24) as a function of Doppler (i.e.  $\mathbf{v}_g^H(f_{\text{nd}})\mathbf{v}_{\bar{g}}(f_{\text{nd}})$  for  $g \neq \bar{g}$ ), is actually not physically meaningful in the staggering context because it does not

account for decoherence from range misalignment (see Sect. III.B.2).

While a relational assessment between Doppler manifolds is not physically meaningful, the evaluation in (20)-(22) can still be applied within each range interval. Specifically, again denoting  $\tilde{G} = G - g$ , generalize (20) using (24) and (7) as

$$\begin{aligned} u_g(f_{\text{nd}}) &= \mathbf{v}_g^H(f_{\text{nd}})\mathbf{v}_g(f_{\text{nd}}) \\ &= \sum_{m=1}^M e^{-j2\pi f_{\text{nd}} \varepsilon_{\text{acc}}(\tilde{G}+m)} \\ &= \sum_{m=1}^M e^{-j2\pi (\tilde{G}+m-1)f_{\text{nd}}} e^{-j2\pi f_{\text{nd}} \Delta \varepsilon_{\text{acc}}(\tilde{G}+m)}, \end{aligned} \quad (30)$$

which could be assessed using (21) or (22). Since each range interval has distinct staggering/STC, with ensuing misalignment decoherence, it is not yet clear if an analytical generalization of (21) or (22) exists that can properly aggregate the set of MTA incoherent responses together with the integrated sidelobes from the range-aligned interval, thereby producing an ‘‘MTA total’’ version of IDSL or EDSL. With that said, Sect. IV uses canonical examples to illustrate how the degree of staggering drives the amount of relative decoherence, which manifests as smearing.

### C. PDiD Implications for MIMO Radar

Given that STC is well-known to bolster separability for MIMO radar [13-18], it stands to reason that staggering may provide additional freedom via Doppler diversification. Consequently, consider  $P$  emitters, each generating a CPI of  $M$  pulses, where (for simplicity) the first pulse is synchronized across the  $p = 1, \dots, P$  emitters while the remaining  $M - 1$  pulses in each sequence possess independent staggering. We shall likewise maintain the same CPI extent across all emitters for ease of comparison and to later (in Sect. III) infer aspects of staggering limits. Of course, further generalization is possible by relaxing this condition. For the  $p$ th emitter,  $s_p(t)$  is the distinct transmitted waveform repeated over the CPI and  $\theta_{p,m}$  is the STC phase on the  $m$ th pulse, with  $\Delta \varepsilon_{\text{acc},p}(m) = T_{\text{acc},p}(m)/T_{\text{avg}}$  the phase-slope deflection and  $T_{\text{acc},p}(m)$  the associated time accumulated prior to the  $m$ th PRI. Note that MTA responses are not considered here, though the two formulations are compatible.

The PRI stagger sequences are unique across the  $P$  emitters, thus necessitating receive alignment across the  $M$  PRIs for each emitter. We can generalize the  $m$ th PRI interval in (10) relative to the  $\bar{p}$ th emitter in this MIMO context as

$$y_{\bar{p}}(m, t) = \eta_m(t) \times \left( \sum_{f_D} \left[ s_{\bar{p}}(t; f_D) * \hat{x}_{\bar{p}}(t; f_D) \right] e^{j[2\pi f_{\text{ND}} \varepsilon_{\text{acc}, \bar{p}}(m) + \theta_{\bar{p}, m}]} + \sum_{\substack{p=1 \\ p \neq \bar{p}}}^P \sum_{f_D} \left[ s_p(t; f_D) * \tilde{x}_p(t; f_D) \right] e^{j[2\pi f_{\text{ND}} \varepsilon_{\text{acc}, p}(m) + \theta_{p, m}]} + n_{\bar{p}}(m, t) \right). \quad (31)$$

Here  $\hat{x}_{\bar{p}}(t; f_D) = x_{\bar{p}}(t + \Delta T_{\text{acc}, \bar{p}}(m); f_D)$  for delay offset  $\Delta T_{\text{acc}, \bar{p}}(m) = T_{\text{acc}, \bar{p}}(m) - (m-1)T_{\text{avg}} = \Delta \varepsilon_{\text{acc}, \bar{p}}(m) T_{\text{avg}}$  is the range-aligned scattering by direct extension of (6) and (7), while  $\tilde{x}_p(t; f_D) = x_p(t + \Delta T_{\text{acc}, p, \bar{p}}(m); f_D)$  for delay offset  $\Delta T_{\text{acc}, p, \bar{p}}(m) = T_{\text{acc}, \bar{p}}(m) - T_{\text{acc}, p}(m) = \Delta T_{\text{acc}, \bar{p}}(m) - \Delta T_{\text{acc}, p}(m)$  is the misaligned scattering for each emitter  $p \neq \bar{p}$ , with  $n_{\bar{p}}(m, t)$  the  $\bar{p}$ th aligned noise. Note that  $t = 0$  for  $y_{\bar{p}}(m, t)$  is based on the beginning of the  $m$ th PRI for a hypothetical uniform case that serves as common reference for all emitters.

The term  $\eta_m(t)$  in (31) generalizes the  $\text{rect}[\tau, T_m]$  term in (1), (10), and (23) to account for collective T-R switching across all  $P$  emitters, isolating the portion of the  $m$ th PRI for which no pulse transmission is occurring and thus no direct-path leakage saturates any receivers, assuming negligible propagation delay between platforms (but may require consideration for some configurations). For now, assume the maximum stagger amount is much less than the pulsewidth (i.e.  $\delta \ll \tau$ ). Recalling as well that each stagger value  $T_{p, m}$  is drawn from the symmetric uniform distribution  $[-\delta, +\delta]$  centered on  $T_{\text{avg}}$  (i.e. positive/negative deviation is equally likely), then it stands to reason that the observation interval within the  $m$ th PRI occurs after the latest transmitting pulse (across the  $P$  emitters) and before the earliest transmitting pulse within the  $(m+1)$ th PRI across the  $P$  emitters. Consequently, we can define

$$\eta_m(t) = \left\lfloor \frac{1}{P} \sum_{p=1}^P \text{rect} \left[ \left( \Delta \varepsilon_{\text{acc}, p}(m) T_{\text{avg}} + \tau \right), \left( \Delta \varepsilon_{\text{acc}, p}(m) T_{\text{avg}} + T_{p, m} \right) \right] \right\rfloor, \quad (32)$$

in which floor operation  $\lfloor \bullet \rfloor$  applied to the average of time-offset  $\text{rect}[\bullet]$  functions is unity only when all  $P$  observation windows coincide, and zero otherwise. The impact of this arrangement is discussed in Sect. III.

If the  $\delta \ll \tau$  assumption does not hold, then the PRI intervals for different emitters become intermingled. This situation would require a given receiver to possess sufficient isolation between the other transmitters (to prevent complete loss of the range observation interval) and/or compensation methods to address eclipsing such as discussed for MTA.

Similar to (24), we can likewise generalize (11)-(13) to define an  $M \times 1$  normalized Doppler steering vector for each emitter as

$$\mathbf{v}_p(f_{\text{ND}}) = \begin{bmatrix} 1 & e^{j[2\pi f_{\text{ND}} \varepsilon_{\text{acc}, p}(2) + \theta_{p, 2}]} \\ \dots & e^{j[2\pi f_{\text{ND}} \varepsilon_{\text{acc}, p}(M) + \theta_{p, M}]} \end{bmatrix}^T \quad (33) \\ = \bar{\mathbf{v}}(f_{\text{ND}}) \odot \mathbf{d}(f_{\text{ND}}; \Delta \varepsilon_{\text{acc}, p}, \boldsymbol{\theta}_p),$$

which has distinct STC sequence  $\boldsymbol{\theta}_p$  and phase-slope deflection sequence  $\Delta \varepsilon_{\text{acc}, p}$ . Performing pulse compression on (31), which means applying  $\bar{p}$ th matched/mismatched filter  $h_{\bar{p}}(t)$  and recalling eclipsing effects near observation window edges, then yields

$$z_{\bar{p}}(m, t) = h_{\bar{p}}(t) * y_{\bar{p}}(m, t) \\ \approx \sum_{f_D} \left[ h_{\bar{p}}(t) * s_{\bar{p}}(t; f_D) * \hat{x}_{\bar{p}}(t; f_D) \right] e^{j[2\pi f_{\text{ND}} \varepsilon_{\text{acc}, \bar{p}}(m) + \theta_{\bar{p}, m}]} \\ + \tilde{n}_{\bar{p}}(m, t) + \sum_{\substack{p=1 \\ p \neq \bar{p}}}^P \sum_{f_D} \left[ h_{\bar{p}}(t) * s_p(t; f_D) * \tilde{x}_{p, \bar{p}}(t; f_D) \right] \\ \times e^{j[2\pi f_{\text{ND}} \varepsilon_{\text{acc}, p}(m) + \theta_{p, m}]} \quad (34) \\ \approx \sum_{f_D} \left[ \tilde{x}_{\bar{p}}(t; f_D) \right] e^{j[2\pi f_{\text{ND}} \varepsilon_{\text{acc}, \bar{p}}(m) + \theta_{\bar{p}, m}]} + \tilde{n}_{\bar{p}}(m, t) \\ + \sum_{\substack{p=1 \\ p \neq \bar{p}}}^P \sum_{f_D} \tilde{\alpha}_{p, \bar{p}}(t; f_D) e^{j[2\pi f_{\text{ND}} \varepsilon_{\text{acc}, p}(m) + \theta_{p, m}]} \\ \approx \tilde{\psi}_{\bar{p}}(m, t) + \tilde{n}_{\bar{p}}(m, t) + \sum_{\substack{p=1 \\ p \neq \bar{p}}}^P \tilde{\psi}_{p, \bar{p}}(m, t).$$

Here the  $\tilde{x}_{\bar{p}}(t; f_D)$  term is the range-aligned scattering  $\tilde{x}_{\bar{p}}(t; f_D)$  shaped by response  $r_{\bar{p}}(t; f_D) = h_{\bar{p}}(t) * s_{\bar{p}}(t; f_D)$  from the  $\bar{p}$ th waveform and matched/mismatched filter that realizes a coherent integration gain of  $\tau B$  just like (17) when  $f_D$  is sufficiently small, and otherwise accounting for Doppler mismatch loss. In contrast, the term  $\tilde{\alpha}_{p, \bar{p}}(t; f_D)$  is the scattering  $\tilde{x}_{p, \bar{p}}(t; f_D)$  induced by the  $p$ th emitter (for  $p \neq \bar{p}$ ) and range misaligned relative to the  $\bar{p}$ th staggering sequence, which is subsequently shaped by cross-correlation  $c_{p, \bar{p}}(t; f_D) = h_{\bar{p}}(t) * s_p(t; f_D)$  between the  $p$ th waveform and  $\bar{p}$ th pulse compression filter. If the same waveform is employed across all  $P$  emitters, then the simplification  $c_{p, \bar{p}}(t; f_D) = r_{\bar{p}}(t; f_D)$  occurs. Regardless, due to range misalignment, all  $p \neq \bar{p}$  terms are incoherent across the CPI. Like the MTA framework (Sect. II.B), the final line in (34) therefore consists of coherent scattering for the  $\bar{p}$ th emitter in  $\tilde{\psi}_{\bar{p}}(m, t)$  after subsuming the staggering/STC phase component, the similar collection of incoherent responses

$\check{\Psi}_{p,\bar{p}}(m,t)$  for the other  $(P-1)$  emitters, and pulse compressed noise  $\check{n}_{\bar{p}}(m,t)$  for the given range alignment.

Using (34) we again leverage (18) to write an I/Q sampled and Doppler discretized version that is range-aligned for the  $\bar{p}$ th emitter as

$$\begin{aligned} \mathbf{z}_{\bar{p}}(\ell) &= \sum_{f_D} \check{\mathbf{x}}_{\bar{p}}(\ell; f_D) \mathbf{v}_{\bar{p}}(f_{nD}) \\ &+ \sum_{\substack{p=1 \\ p \neq \bar{p}}}^P \sum_{f_D} [\check{\mathbf{a}}_{p,\bar{p}}(\ell; f_D) \odot \mathbf{v}_p(f_{nD})] + \check{\mathbf{n}}_{\bar{p}}(\ell) \quad (35) \\ &\approx \mathbf{V}_{\bar{p}} \check{\mathbf{x}}_{\bar{p}}(\ell) + \sum_{\substack{p=1 \\ p \neq \bar{p}}}^P [\check{\mathbf{A}}_{p,\bar{p}}(\ell) \odot \mathbf{V}_p] \mathbf{1}_{N \times 1} + \check{\mathbf{n}}_{\bar{p}}(\ell). \end{aligned}$$

Here  $\mathbf{V}_{\bar{p}}$  is the  $M \times N$  discretized Doppler matrix for the staggering/STC sequences of the  $\bar{p}$ th emitter, with corresponding  $N \times 1$  vector  $\check{\mathbf{x}}_{\bar{p}}(\ell)$  collecting the values  $\check{x}_{\bar{p}}(\ell; f_D)$  across discretized Doppler. The  $M \times 1$  vector  $\check{\mathbf{a}}_{p,\bar{p}}(\ell; f_D)$  collects discretized versions of the incoherent/cross-correlated values  $\check{a}_{p,\bar{p}}(t; f_D)$  over the  $M$  PRIs, with further collection across the  $N$  discretized Doppler values yielding  $M \times N$  incoherent scattering matrix  $\check{\mathbf{A}}_{p,\bar{p}}(\ell)$ . The remaining combination with discretized Doppler matrix  $\mathbf{V}_p$  and subsequent summation via multiplication by the  $\mathbf{1}_{N \times 1}$  vector follow the same manner as (28). Also like the MTA model, misaligned scattering due to the  $p \neq \bar{p}$  emitters in (35) would similarly be perceived as uncorrelated noise in slow-time, though the spatial dependence of each component would rely on the location/orientation of the corresponding transmit/receive antennas and scattering.

An important distinction between the MTA model in (28) and MIMO model in (35) is that the latter may involve distinct waveforms across the  $P$  emitters, yielding a combination of range-focused responses via  $r_{\bar{p}}(t; f_D)$  that achieve coherent integration gain and unfocused responses via  $c_{p,\bar{p}}(t; f_D)$  that do not experience pulse compression gain. In other words, the clutter generated by the other  $(P-1)$  emitters is lessened by  $\sim \tau B$  relative to what it would be if range-focused. Of course, that does not mean MIMO clutter components are negligible since common spectral support dictates their achievable cross-correlation separability be on the order of  $\sim 1/(\tau B)$  [9], and because clutter is pervasive and often relatively high power.

Similar to the MTA arrangement, we could conceivably perform range realignment from the stagger sequence of emitter  $\bar{p}$  to that of emitter  $\check{p} \neq \bar{p}$  in the same manner as (29). And since  $c_{p,\bar{p}}(t; f_D)$  is consistent across the CPI, the fact that no pulse compression focusing has been achieved does not prevent clutter cancellation from being performed (e.g. [40]). Consequently, a sequential process of range realignment and clutter cancellation for each of the  $p$  responses could in

principle be performed in the same way as Sect. II.B for distinct range ambiguities, still being mindful of range interval edge effects.

Finally, we can again generalize (20), albeit now using (33), to obtain

$$\begin{aligned} u_p(f_{nD}) &= \mathbf{v}_p^H(f_{nD}) \mathbf{v}_p(f_{nD} = 0) \\ &= \sum_{m=1}^M e^{-j2\pi f_{nD} \epsilon_{\text{acc},p}(m)} \\ &= \sum_{m=1}^M e^{-j2\pi(m-1)f_{nD}} e^{-j2\pi f_{nD} \Delta \epsilon_{\text{acc},p}(m)}, \quad (36) \end{aligned}$$

which could be assessed using (21) or (22). It should be noted that, like the MTA case, relational assessment between Doppler manifolds for different emitters (e.g.  $\mathbf{v}_p^H(f_{nD}) \mathbf{v}_{\bar{p}}(f_{nD})$  for  $p \neq \bar{p}$ ) is not physically meaningful when staggering is involved because doing so does not account for decoherence. Sect. IV uses canonical examples to illustrate the relationship between staggering and the resulting MIMO decoherence, which like MTA manifests as smearing.

### III. PARAMETERIZATION CONSIDERATIONS FOR PDiD

Beyond the ability to make different range ambiguities and MIMO emitters more or less separable on receive, the choice of STC is essentially arbitrary from a feasibility perspective. Staggering, on the other hand, introduces “bookend” effects in which performance trade-offs can arise if the degree of staggering is either too great or too small. Within this PDiD framework we consider some of these limits.

#### A. Practical Upper Limits on Staggering

Per (5), random values of  $\Delta T_m$  for  $m > 0$  are independently drawn from the interval  $[-\delta, +\delta]$ . Therefore, the shortest possible staggered PRI of  $T_{\min} = T_{\text{avg}} - \delta$  establishes the smallest observable range swath of  $R_{\min \text{ swath}} = c(T_{\min} - \tau)/2$  meters, for speed of light  $c$  and pulsewidth  $\tau$ . The longest possible staggered PRI of  $T_{\max} = T_{\text{avg}} + \delta$  contains the largest range swath of  $R_{\max \text{ swath}} = c(T_{\max} - \tau)/2 = R_{\min} + 2\delta c/2$  meters, though the excess portion is extraneous because receive data is not available across all PRIs. Thus, at the far end of the range interval a portion amounting to

$$R_{\text{loss}} = c(T_{\text{avg}} - T_{\min})/2 = \delta c/2 \quad (37)$$

is essentially lost relative to a uniform PRI, though missing pulse or interpolation receive processing methods [38,39] could conceivably be employed at these ranges.

Put another way, staggering realizes a reduction of  $[1 - (T_{\min} - \tau)/(T_{\text{avg}} - \tau)] = \delta/(T_{\text{avg}} - \tau) = \bar{\delta}/(1 - \chi)$  percent in observable range swath relative to the average observable swath of  $R_{\text{avg swath}} = c(T_{\text{avg}} - \tau)/2$  associated with uniform PRI, where  $\bar{\delta} = \delta/T_{\text{avg}}$  is the normalized stagger limit and  $\chi = \tau/T_{\text{avg}}$  is the duty cycle for uniform PRI. Alternatively, we

could say that staggering within  $\pm\bar{\delta}$  reduces the meaningful PRI interval (i.e. now inclusive of pulsewidth) by

$$\begin{aligned} \% \text{ range loss} &= [1 - T_{\min}/T_{\text{avg}}] \\ &= [1 - (T_{\text{avg}} - \delta)/T_{\text{avg}}] = \bar{\delta} \text{ percent,} \end{aligned} \quad (38)$$

providing a convenient direct relationship.

### A.1. Staggering Upper Limits for MTA

Based on the MTA generalization in Sect. II.B, we can further extend this consideration of observable range swath. Figures 4 and 5 illustrate examples of two extreme cases of staggering, with all other possibilities lying between these extremes for a fixed  $\delta$  limit. Specifically, for  $G = 3$  range ambiguity intervals,  $M = 7$  pulses in the CPI, and 9 overall pulses (so  $G - 1 = 2$  fill pulses), one example has the maximum stagger  $T_{\text{avg}} + \delta$  repeated until the minimum stagger  $T_{\text{avg}} - \delta$  must then be repeated so the sum of staggers remains zero (i.e. to maintain constant CPI extent). The other example involves the opposite (i.e. repeated minimum followed by necessary repeated maximum).

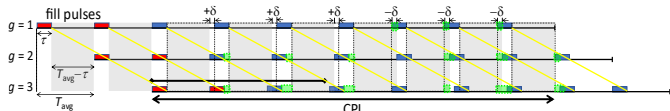


**Fig. 4.** Max-then-min staggering arrangement for  $G = 3$  range ambiguities, with fill pulses in red, CPI pulses in blue, gray regions the observation intervals for hypothetical uniform PRIs, yellow diagonals help visualize propagation, and the dashed black boxes outlining the actual observation intervals due to staggering, with green regions depicting the resulting range loss intervals due to T-R switching. Note that simple extension of the CPI could capture the lost range intervals at the very end since another pulse is not transmitted.

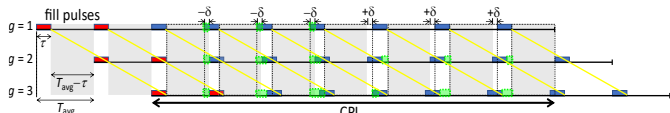


**Fig. 5.** Min-then-max staggering arrangement for  $G = 3$  range ambiguities, with fill pulses in red, CPI pulses in blue, gray regions the observation intervals for hypothetical uniform PRIs, yellow diagonals help visualize propagation, and the dashed black boxes outlining the actual observation intervals due to staggering, with green regions depicting the resulting range loss intervals due to T-R switching.

Here red blocks denote fill pulses, blue blocks indicate pulses in the CPI, gray boxes indicate what would be the extent of a uniform PRI relative to each pulse, and the yellow diagonals help visualize the propagation of each pulse in time. The dashed black boxes outline the resulting observation interval for each PRI, noting that the T-R switching operation only corresponds to the  $g = 1$  interval (i.e. pulses depicted for  $g = 2$  and 3 are provided to show relative time offsets). The fill pulses here employ a uniform PRI so staggering is only performed during the CPI to facilitate direct comparisons (though this need not be the case in practice). The ensuing green regions show the portion(s) of each PRI that is/are lost due to T-R switching. While it is conceivable that simultaneous transmit and receive (STAR) operation (e.g. [41,42]) could alleviate this effect, doing so involves other

technical hurdles, so it is instructive to consider the impact when STAR is not available.

We can make some general inferences from these extreme MTA examples. The first is that range interval  $g = 1$  realizes observable range swath loss  $R_{\text{loss}, g=1} = c(T_{\text{avg}} - T_{\min})/2 = \delta c/2$ , which is precisely the same as (37) and is likewise the same for both examples. For the  $g = 2$  and 3 range intervals in both figures we see the impact of the “turn over” point in the middle where the maximum/minimum stagger changes to the opposite. Specifically,  $g = 2$  in both cases experiences a  $2\delta$  loss at the far end of this range interval and a  $\delta$  loss at the near end. Likewise,  $g = 3$  experiences a  $3\delta$  loss at the far end and a  $2\delta$  loss at the near end.

We can generalize these observations, while also converting into range, by stating the worst-case loss of

$$R_{\text{far-loss}, g} = (c/2)g\delta \quad (39)$$

at the far end of the  $g$ th range swath, and the worst-case loss of

$$R_{\text{near-loss}, g} = (c/2)(g-1)\delta \quad (40)$$

at the near end of the  $g$ th range swath. Thus the total worst-case loss for the  $g$ th range swath is

$$R_{\text{total-loss}, g} = (c/2)(2g-1)\delta. \quad (41)$$

In other words, staggering produces an increase in the footprint of *blind ranges* due to T-R switching, when imposing the condition that all PRIs must be available for slow-time processing. Note that oscillating between maximum and minimum staggers does not impact these bounds and there is no dependence on the number of pulses as long as  $M > 2g$ . Consequently, these range swath losses to the observation intervals may be acceptable if  $\delta$  is sufficiently modest. For instance, converting the collective worst-case time offsets to normalized values via division by  $T_{\text{avg}}$  realizes the losses in percentage form, where the far, near, and total bounds then become  $g\bar{\delta}$ ,  $(g-1)\bar{\delta}$ , and  $(2g-1)\bar{\delta}$  percent, respectively, for  $\bar{\delta} = \delta/T_{\text{avg}}$ . And again, missing pulse or interpolation methods [38,39] could conceivably be used to compensate.

### A.2. Staggering Upper Limits for MIMO

To assess upper staggering limits for MIMO we employ the same extreme examples considered for MTA. Figure 6 shows stagger arrangements for  $P = 3$  different emitters, two of which follow the max-to-min (here red pulses) or min-to-max (here green pulses) sequences from Figs. 4 and 5, respectively, albeit now for a single range ambiguity ( $g = 1$ ). The other emitter in Fig. 6 (blue pulses) has a uniform PRI, which for the assessment of range interval loss also establishes a common reference for illustration purposes. The receive interval for each of these pulse sequences is likewise color-coded as red, green, and blue, though with transparent boxes. Consequently, when all three receive intervals coincide the color is gray, and further identified with the dashed black box, to denote the observation intervals in which there is no direct-path leakage

between platforms (i.e. the coincident observation interval determined by (32)).

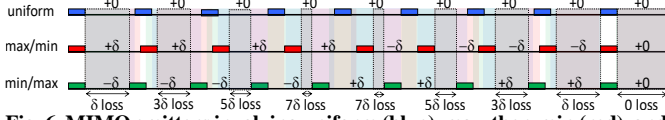


**Fig. 6.** MIMO emitters involving uniform (blue), max-then-min (red), and min-then-max (green) staggering arrangements, with black dashed boxes indicating the available observation intervals free of any direct path transmitter leakage, and thereby highlighting the associated range interval losses.

For this  $M = 9$  pulse example the two staggered cases each possess four PRIs of extent  $T_{\text{avg}} + \delta$  and four PRIs of extent  $T_{\text{avg}} - \delta$ , albeit in opposite order, with the final PRI of extent  $T_{\text{avg}}$  to preserve the same CPI extent. For  $M$  even, the final uniform PRI could be omitted while the difference extremes would remain the same. We therefore find that the interval losses progress as  $\delta, 3\delta, 5\delta, 7\delta$  until reaching the center of the CPI. Given these extremes, the range extent of the observation interval available across the entire CPI is therefore

$$R_{\text{MIMO-obs}} = \max\left\{0, \left[(T_{\text{avg}} - \tau) - (2\lfloor M/2 \rfloor - 1)\delta\right]\right\} \times c/2, \quad (42)$$

which is the smallest remaining over the sequence of interval losses due to T-R switching and could clearly become nonexistent. The floor operation in (42) ensures applicability for both even and odd  $M$ . Normalizing the bracketed portion of (42) by  $T_{\text{avg}}$  again provides a percentage perspective as

$$\text{observation \%} = \max\left\{0, \left[(1 - \chi) - (2\lfloor M/2 \rfloor - 1)\bar{\delta}\right]\right\}, \quad (43)$$

where the maximum of  $(1 - \chi)$  percent occurs if all emitters have a uniform PRI.

For instance, for  $\bar{\delta} = 2$  percent and duty cycle  $\chi = 10$  percent these extreme stagger sequences would reduce the observation interval from 90 percent (identical uniform PRIs) to 0 percent if  $M$  exceeds 45 pulses. However, if  $\bar{\delta} = 20$  percent with the same duty cycle, the observation interval reaches 0 percent when  $M$  exceeds only 5 pulses. While random staggering would clearly lie somewhere between uniform staggering and the combination of these extreme cases, this prospective loss in observation range implies that there is clearly a practical upper limit on  $\bar{\delta}$ , not withstanding the prospect of STAR [41,42] and/or realizing adequate receive isolation.

### B. Practical Lower Limits on Staggering

While loss of observable range swath can certainly produce a downward design pressure on the value of  $\delta$ , there is also an upward design pressure stemming from *i)* the desired suppression of Doppler ambiguities and/or *ii)* achieving scattering discrimination via decoherence for different MTA intervals or MIMO responses. In that regard, using (7) we can write the complete slow-time phase of the  $m$ th element of the steering vector in (11) as

$$\phi_m(f_{\text{ND}}) = 2\pi(m-1)f_{\text{ND}} + 2\pi\Delta\epsilon_{\text{acc}}(m)f_{\text{ND}} + \theta_m, \quad (44)$$

where the first term is the standard Vandermonde form via (12), the second term is the Doppler-dependent phase deviation from staggering, and the third term is the STC phase constant. Because both are linearly dependent on normalized Doppler we can formalize a uniform-referenced ‘‘Doppler-to-phase slope’’ based on the first term as

$$m\text{th slope} = \frac{2\pi(m-1)f_{\text{ND}}}{2\pi f_{\text{ND}}} = (m-1) \quad (45)$$

and a ‘‘slope deflection’’ based on the second term as

$$m\text{th slope deflection} = \frac{2\pi\Delta\epsilon_{\text{acc}}(m)f_{\text{ND}}}{2\pi f_{\text{ND}}} = \Delta\epsilon_{\text{acc}}(m). \quad (46)$$

We again find that extreme cases occur when maximum or minimum staggers are repeated until the opposite is required to preserve constant CPI extent. Specifically, noting phase slopes are based on time accumulation from previous PRIs, these extreme cases realize  $\Delta\epsilon_m = \pm\bar{\delta}$  so (46) yields

$$\Delta\epsilon_{\text{acc}}(m) = \pm(m-1)\bar{\delta} \quad (47)$$

via (7) for pulse indices  $m = 2, \dots, \bar{m}$ , with  $\bar{m} = \lfloor M/2 \rfloor + 1$ . The remaining  $m = \bar{m} + 1, \dots, M$  indices necessarily have  $\Delta\epsilon_m = \mp\bar{\delta}$  (opposite sign) to maintain CPI extent, thereby resulting in

$$\Delta\epsilon_{\text{acc}}(m) = \pm(\bar{m}-1)\bar{\delta} \mp (m-\bar{m})\bar{\delta}, \quad (48)$$

with  $\Delta\epsilon_{\text{acc}}(M) = 0$  if  $M$  is odd and  $\Delta\epsilon_{\text{acc}}(M) = \pm\bar{\delta}$  if  $M$  is even (and the final PRI providing  $\mp\bar{\delta}$ ). Because  $(\bar{m}-1) \geq (m-\bar{m})$ , with equality only met when  $m = M$  and  $M$  is odd, the largest possible deflection is  $\pm\bar{\delta}(\bar{m}-1)$ , which can occur at  $m = \bar{m}$  and only in these extreme cases. In short, the inter-dependence of staggering values (due to fixed total extent) combined with phase slope deflection dependence on stagger accumulation suggests a nominal amount of staggering is necessary before prospective benefits are achieved.

For example, let the uniform PRI result for  $M = 50$  pulses in Fig. 7 serve as a baseline, where we observe a ‘‘fan plot’’ comprised of the first seven phase slopes (unwrapped) along with their phase-wrapped versions, in addition to the associated Doppler response. When the phases align, such as clearly occurs at integer normalized frequencies, a coherent replica of the Doppler mainlobe is produced.

In contrast, Fig. 8 shows a similar sequence of plots for  $M = 50$  pulses with a random instantiation of staggers distributed on  $\pm 30$  percent. Some offsets can now be discerned in the unwrapped fan plot, which is easier to see for wrapped phase because alignment does not occur, yielding a flattened Doppler response without significant ambiguities. While  $\pm 30$  percent is a significant amount of staggering, if we produce another instantiation using  $\pm 10$  percent, the benefit to Doppler ambiguity suppression is clearly far less significant. Fig. 9 illustrates this case in which near-alignment occurs at  $f_{\text{ND}} = 1$ ,

with more gradual flattening thereafter at higher Doppler (an effect that is considered in more detail shortly).

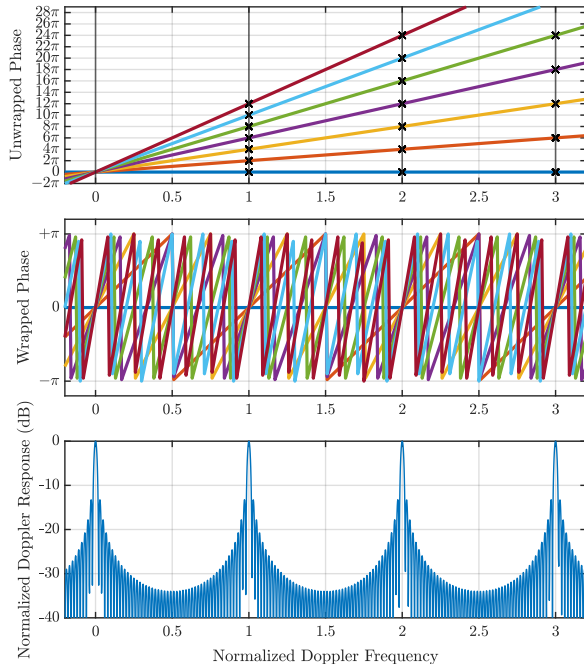


**Fig. 7.** Uniform PRIs and  $M = 50$  pulses yield (top) a “fan plot” of first 7 phase slopes, (middle) wrapped phase for same, and (bottom) resulting Doppler response. As expected for uniform PRIs, we see the repeated Doppler ambiguity (a black ‘x’ indicates where phases perfectly align).

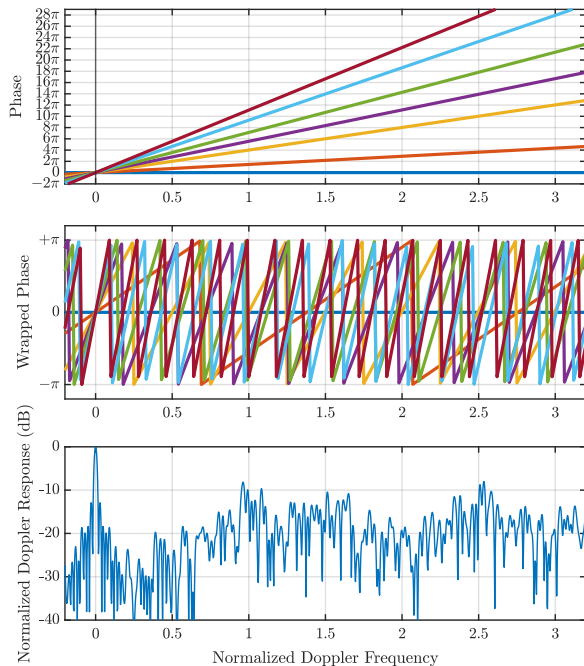


**Fig. 8.** Instantiation of random stagers uniformly distributed on  $\pm 30$  percent and  $M = 50$  pulses yield (top) a “fan plot” of first 7 phase slopes, (middle) wrapped phase for same, and (bottom) resulting Doppler response. Over this Doppler span the wrapped phase slopes do not coalesce to produce significant ambiguities, leading to a flattening of the Doppler response.

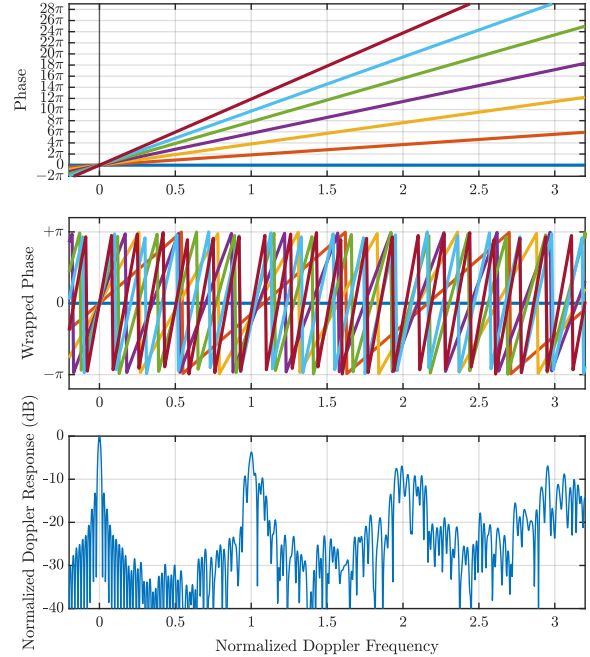


**Fig. 9.** Instantiation of random stagers uniformly distributed on  $\pm 10$  percent and  $M = 50$  pulses yield (top) a “fan plot” of first 7 phase slopes, (middle) wrapped phase for same, and (bottom) resulting Doppler response. With lower slope deflection due to less staggering, higher Doppler is needed before flattening becomes noticeable. At  $f_{nD} = 1$  the wrapped slopes are close to being phase-aligned.

### B.1. Staggering Lower Limits for Doppler Ambiguity

Given the observations above regarding nominal random staggering to suppress Doppler ambiguities, it is instructive to consider average behavior. Per (20), (30), or (36), Appendix B derives the expected zero-referenced Doppler response for  $M$  pulses according to  $\pm \bar{\delta}$  limits on uniformly distributed random staggering. The result of

$$E \left[ \left| \frac{1}{M} u(f_{nD}) \right|^2 \right] = \frac{1}{M} + \frac{2}{M^2} \sum_{m=1}^{M-1} \left( m \cos(2\pi f_{nD}(M-m)) \times \left[ \text{sinc}(2\pi f_{nD} \bar{\delta}) \right]^{(M-m)} \right) \quad (49)$$

from (58) is a function of normalized Doppler  $f_{nD}$  and is invariant to slow-time coding. Figures 10-14 illustrate a few different staggering regimes, with  $\bar{\delta}$  set to 5, 10, 20, 30, and 40 percent, respectively, for  $M = 50$  pulses. In addition, 200 independent trials of random staggering were simulated for each parameterization to confirm (49) via averaging. Note that, aside from a contraction/dilation of Doppler mainlobe/sidelobe widths, these results are qualitatively invariant for different values of  $M$ .

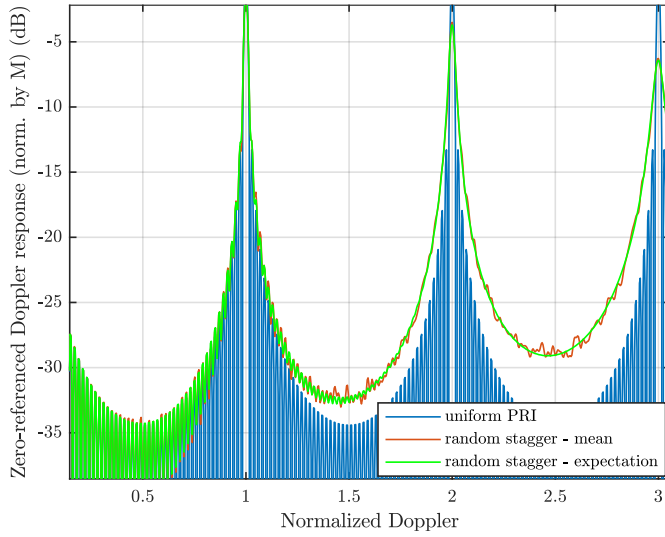


**Fig. 10. Zero-referenced Doppler response from (20) for random staggering within  $\pm 5$  percent**

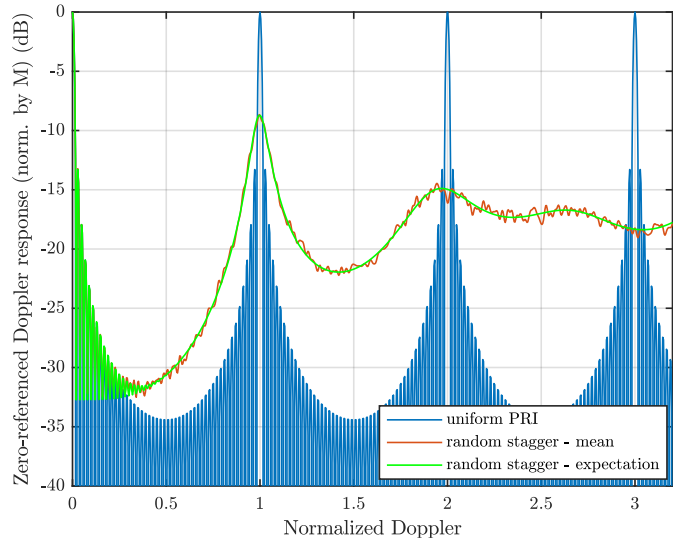


**Fig. 12. Zero-referenced Doppler response from (20) for random staggering within  $\pm 20$  percent**

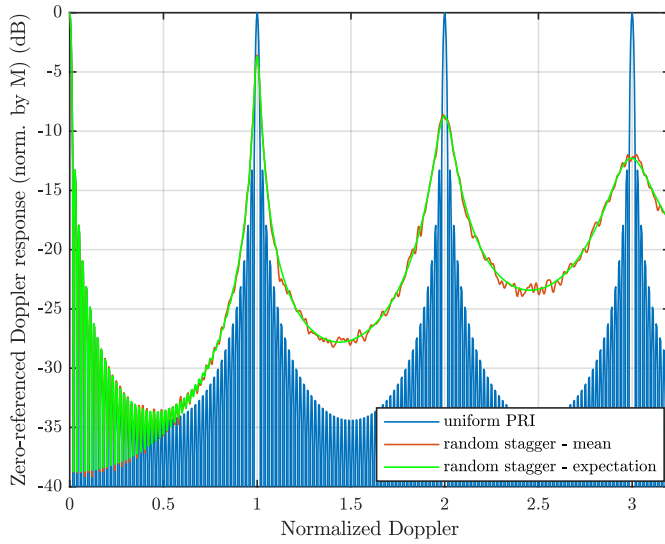


**Fig. 11. Zero-referenced Doppler response from (20) for random staggering within  $\pm 10$  percent**

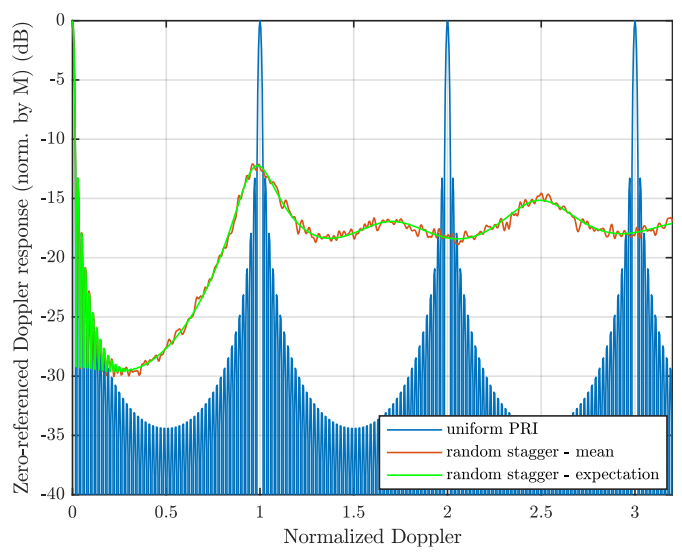


**Fig. 13. Zero-referenced Doppler response from (20) for random staggering within  $\pm 30$  percent**

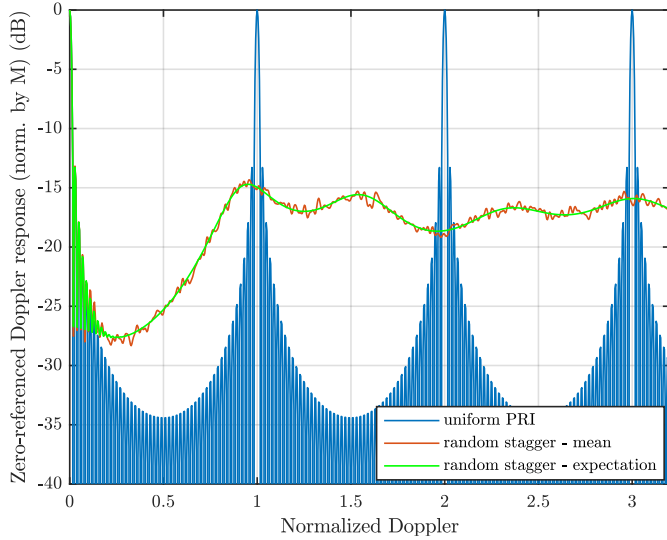


**Fig. 14. Zero-referenced Doppler response from (20) for random staggering within  $\pm 40$  percent**

We can draw some general conclusions from Figs. 10-14. Increasing the allowed amount of staggering (via  $\bar{\delta}$ ) clearly realizes an expected Doppler response that is progressively flatter. Moreover, this flattening approaches  $\sim 1/M$  (converted to dB and normalized to the zero-Doppler peak). This result stands to reason when one considers the expected inner product between two  $M$ -length vectors comprised of independent, random phase values, since that is the very effect being achieved by diversifying Doppler. For  $M = 50$  this value is  $-17$  dB.

Depending on what one deems acceptable for the more prominent expected sidelobe near  $f_{\text{ND}} = 1$ , a reasonable lower limit on  $\bar{\delta}$  may be 30-40 percent since any lower values retain a sharper peak at this Doppler. Beyond  $f_{\text{ND}} = 1$  the average Doppler sidelobes grow flatter as Doppler increases, suggesting that lower  $\bar{\delta}$  could be used if a higher response near  $f_{\text{ND}} = 1$  can be neglected for a given application so that higher Doppler can be perceived without ambiguity. The reason for this effect is readily understood when examining the phase slope behavior (unwrapped and wrapped) in Figs. 7-9, in which small slope deflections yield more meaningful phase differences at higher Doppler.

These more or less nominal values of  $\bar{\delta}$  clearly produce a bounding effect in the MTA and MIMO contexts because avoiding excessive limitations on the available range observation window (per Sects. III.A.1 and III.A.2) contraindicates the use of large staggers. Put another way, staggering for the purpose of expanding the Doppler space may not be practical for MTA or MIMO. However, staggering for the purpose of separability (via decoherence) is considered next.

### B.2. Staggering Lower Limits for Decoherence

To consider the impact of staggering on decoherence for the MTA and MIMO cases it is useful to posit a stationary

impulsive scatterer (IS) at some delay  $T_{\text{IS}}$  and determine how it is affected by relative stagger offsets. Waveform  $s(t)$  would reflect from this impulsive scatterer and then be match filtered on receive, so that the pulse compressed response is simply  $\tilde{x}(t) = x(T_{\text{IS}})r(t - T_{\text{IS}})$ , in which  $r(t - T_{\text{IS}})$  is the delay-shifted waveform autocorrelation and  $x(T_{\text{IS}})$  in this context subsumes the complex scattering and pulse compression gain.

For uniform PRIs or in the original low-PRF monostatic staggering case (with Doppler processing accounting for staggering via (11)), the range-domain response  $\tilde{x}(t) = x(T_{\text{IS}})r(t - T_{\text{IS}})$  remains perfectly aligned (i.e. coherent) across the  $M$  pulses. However, in the MTA/MIMO cases in which different range alignments are possible according to (27) and (34), decoherence-inducing misalignment is dictated by the different points of receive sampling on  $r(t - T_{\text{IS}})$  that occur across the CPI, and therefore is dependent on waveform bandwidth and (to a lesser extent) structure.

Specifically, with range resolution inversely proportional to bandwidth  $B$ , a range misalignment by less than  $\pm 1/B$  across the CPI implies sampling of different points on the pulse compression mainlobe, while greater misalignment realizes sampling of the sidelobes. To illustrate this effect, Fig. 15 depicts a collection of magnitude (middle panel) and phase (lower panel) responses after matched filtering for a variety of different waveforms possessing consistent passband bandwidth (top panel) and associated range resolution. The key take-away here is that phase is essentially constant across the mainlobe, with minor deviation at the edges depending on the particular waveform. Outside the mainlobe, however, significant phase deviation occurs (likewise in a waveform-dependent manner).

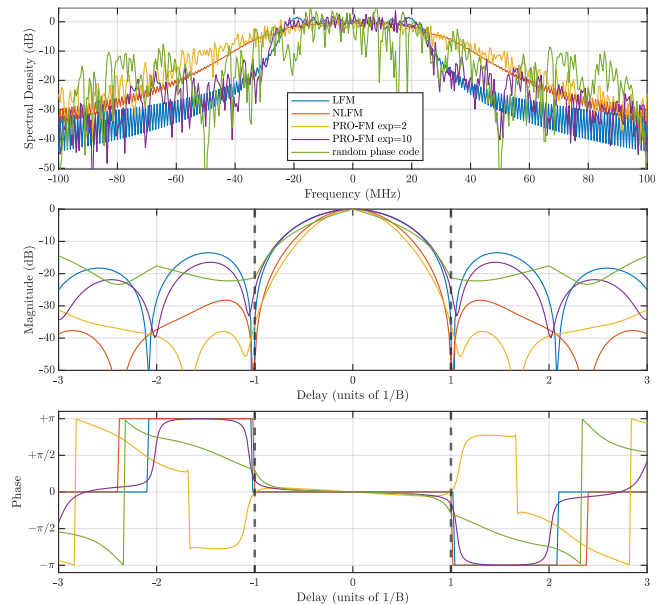


**Fig. 15. Spectral density (top), autocorrelation magnitude (middle) and autocorrelation phase (bottom) for  $\tau B = 50$  waveforms comprising LFM, nonlinear FM (NLFM) [43], instantiations of pseudo-random optimized (PRO) FM based on Gaussian (exponent = 2) [44] and super-Gaussian (exponent = 10) spectral templates [45], and a random polyphase code.**

In other words, if misalignment is less than  $\pm 1/B$ , phase coherency is essentially preserved (though amplitude variation over the mainlobe will play some role as well). When misalignment exceeds  $\pm 1/B$  the more significant magnitude/phase variability over the autocorrelation produces a decoherence effect across slow-time. This observation does suggest a degree of implicit robustness when performing range realignment. Though as we shall see next, this per-PRI view of range alignment does not tell the whole story.

To put this degree of staggering in a meaningful perspective, normalize the nominal  $\pm 1/B$  time shift by  $1/T_{\text{avg}} = \text{PRF}$  so that  $\bar{\delta} \in \pm \text{PRF}/B \times 100$  percent. Then note that, for most radar systems, typical PRF values are on the order of at most 10s of kilohertz (often lower) and typical radar bandwidths are at least a few megahertz (often higher). Using edge values of  $\text{PRF} = 10^4$  Hz and  $B = 10^6$  Hz therefore implies  $\bar{\delta} \in \pm 1$  percent is sufficient to realize misalignment-inducing decoherence from staggering.

Now put this nominal staggering in the context of normalized accumulated staggerer offset  $\Delta \epsilon_{\text{acc}, \tilde{G}} = [\Delta \epsilon_{\text{acc}}(\tilde{G}+1) \ \Delta \epsilon_{\text{acc}}(\tilde{G}+2) \ \cdots \ \Delta \epsilon_{\text{acc}}(\tilde{G}+M)]^T$  for  $\tilde{G} = G - g$  defined in (24) for MTA. If we alternatively denote this vector as  $\Delta \epsilon_{\text{acc}, G-g}$  for the  $g$ th interval, then the degree of decoherence relative to some other  $\bar{g}$ th interval is obtained by examining the values in the vector resulting from

$$g \text{ vs. } \bar{g} \text{ decoherence spread} = (\Delta \epsilon_{\text{acc}, G-g} - \Delta \epsilon_{\text{acc}, G-\bar{g}}), \quad (50)$$

where each term is the relative range offset for a given PRI due to staggering. Since the maximum per-PRI staggering amount is  $\pm \bar{\delta}$  percent, we find that

$$\text{MTA max decoherence spread} = \pm |g - \bar{g}| \bar{\delta} \quad (51)$$

(in percent range) between different ambiguity intervals. In other words, there is a “decoherence amplification” when intervals are non-adjacent, thereby suggesting an even smaller nominal staggering value for those cases. Canonical examples of this phenomenon are provided in Sect. IV.

Similarly examining  $\Delta \epsilon_{\text{acc}, p}$  from (33) for MIMO, the analogous result

$$p \text{ vs. } \bar{p} \text{ decoherence spread} = (\Delta \epsilon_{\text{acc}, p} - \Delta \epsilon_{\text{acc}, \bar{p}}) \quad (52)$$

is obtained, again with each term in this vector the relative range offset for a given PRI due to staggering. Now, however, the staggering sequences can be completely independent, and therefore their accumulated offsets can become quite different. Indeed, if we assign the previous max-then-min and min-then-max extreme cases to two MIMO emitters, then according to (47) the respective center offset values are  $\Delta \epsilon_{\text{acc}}(\bar{m}) = \pm \lfloor M/2 \rfloor \bar{\delta}$  and their difference via (52) is  $\pm 2 \lfloor M/2 \rfloor \bar{\delta}$ , or simply

$$\text{MIMO max decoherence spread} = \pm M \bar{\delta} \quad (53)$$

(in percent range) ignoring the even/odd distinction in number of pulses. Clearly MIMO can experience far greater decoherence amplification than MTA, suggesting that the nominal amount of staggering to realize decoherence is considerably lower.

For instance, Fig. 16 illustrates a Monte Carlo result based on  $10^5$  independent trials of random staggering instantiations for a  $M = 100$  pulse CPI and staggering bound of  $\bar{\delta} = 0.1$  percent (though the response generalizes to arbitrary  $\bar{\delta}$  due to normalization). All CPIs are forced to have the same extent by introducing additional random perturbations in an iterative manner until the requisite fixed extent is attained (it has been verified that the statistical properties are preserved by this approach). For the heatmap perspective in Fig. 16 the  $m$ th column in the image is a histogram of accumulated staggering values at the  $m$ th PRI, where the left/right endpoints are zero due to fixed CPI extent and the offset accumulation has been normalized by  $(M/2)\bar{\delta}$ . The white diamond outline corresponds to the bounding extremes, which are likewise normalized. Determining the standard deviation for the center histograms, which are all well-fit by a Gaussian distribution, reveals that 99 percent of accumulated staggering (i.e. 3 standard deviations) lie within  $\pm 21$  percent of the bounds that exist at  $\pm (M/2)\bar{\delta}$ . In other words, it is highly unlikely that even a significant fraction of the extreme bounds will be realized for completely random staggering (and a pseudo-random approach could guarantee practical limits). Further canonical examples are provided in Sect. IV.

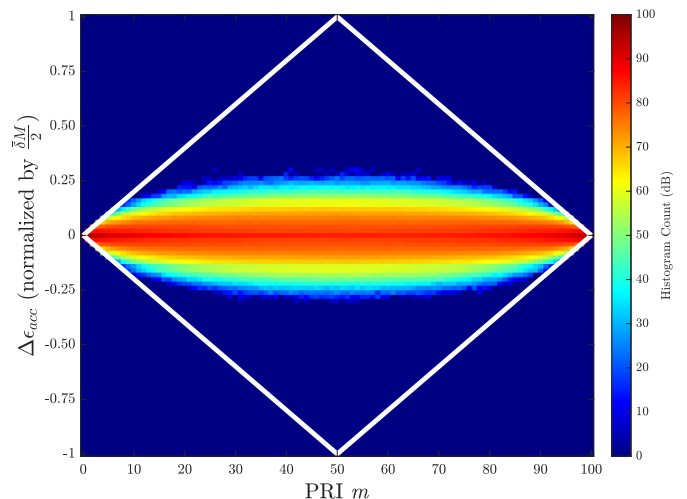


**Fig. 16.** Monte Carlo histogram of accumulated staggering of each PRI for  $10^5$  independent trials of random staggering with  $M = 100$  pulses, fixed CPI length, and  $\bar{\delta} = 0.1$  percent (response generalizes to arbitrary  $\bar{\delta}$  due to normalization)

There are a couple additional considerations arising from the above observation of MIMO staggering sensitivity caused by decoherence amplification. The first is that range realignment from one emitter to another may need to be more precise than was previously inferred from Fig. 15 based on per-PRI phase coherence across the pulse compression mainlobe.

The other consideration is that eclipsing effects are more prevalent for MIMO (per Fig. 6), introducing a nonstationarity that realignment alone cannot address, again suggesting a more pseudo-random approach whereby MIMO stagger sequences are designed based on diversification while tempering eclipsing.

#### IV. CANONICAL DECOHERENCE EXAMPLES

Given the inherent complexity of the PDiD arrangement, especially within the context of MTA or MIMO, we shall limit attention here to canonical examples that help explain the phenomenological behavior, leaving more realistic representations of scattering environments (and open-air measurements thereof) for the sequel, though some is illustrated in [1]. Consequently, the following examples show the responses from a few simple point scatterers in the absence of clutter or noise, with the understanding that the ensuing effects directly extend to real scenarios, which can be viewed as the superposition of an infinite collection of point scatterers. In each case, receive processing is performed using complete knowledge of the transmit parameters.

##### A. Decoherence Examples for MTA

To illustrate decoherence in the MTA context, consider  $M = 100$  pulses modulated with an LFM waveform having  $\tau B = 50$ , and three distinct point scatterers that reside in  $G = 3$  different range ambiguity intervals for the given PRF, with specific parameters in Table I. Scatterers are each scaled to produce a unity amplitude at the matched point following pulse compression and Doppler processing (when coherent). Oversampling is performed in range by a factor of 4 (relative to 3-dB bandwidth) and in Doppler by  $K = 10$ .

**Table I. Apparent and actual range/Doppler locations of canonical MTA point scatterers**

	Scatterer	Scatterer	Scatterer
actual range ambiguity ( $g$ )	1	2	3
apparent range index	1600	400	900
actual range index	1600	2400	4900
normalized Doppler	$+\pi/4$	$-\pi/2$	$+\pi/3$

It is instructive to first compare behavior between the use of STC alone and full PDiD operation. The inclusion or not of STC with non-negligible staggering produces a more modest difference in behavior, which is illustrated further below. Fig. 17 depicts these three range-ambiguous intervals for uniform PRI with and without STC. The non-STC case (bottom panel) clearly shows coherent focusing of all three scatterers, which represents standard radar operation in which range ambiguities fold over in an indistinguishable manner. The use of STC to discriminate MTA [34-37] (top panel) introduces a decoherence in slow-time, which translates into a smearing

across Doppler when not focused to the given range ambiguity of interest. Here we are matching to the 1<sup>st</sup> interval so the scatterer at range index 1600 (both apparent and true) is slow-time focused, while the folded scatterers from the 2<sup>nd</sup> and 3<sup>rd</sup> intervals (at apparent range indices 400 and 900) are not.

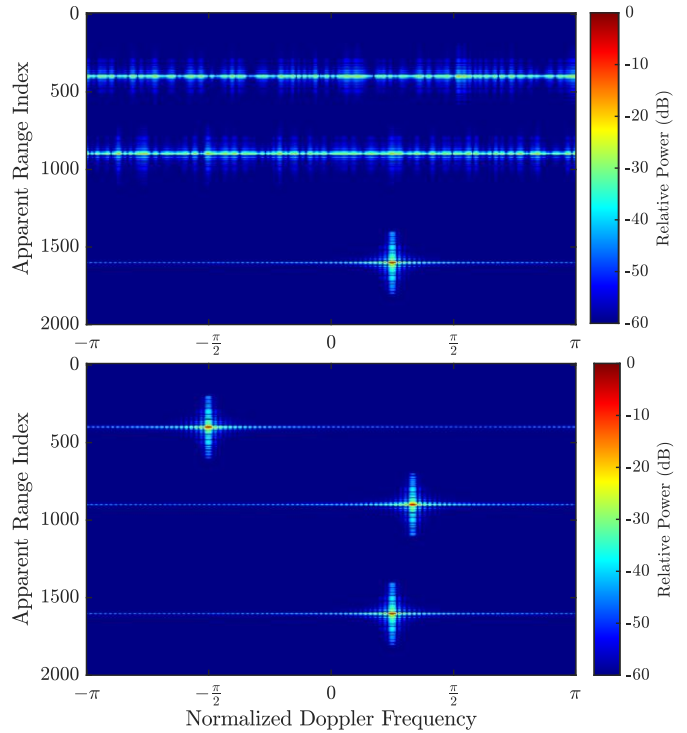


**Fig. 17. Canonical example of 3 scatterers in different range ambiguities for uniform PRIs, (top) with STC and (bottom) without STC, when matching to the 1<sup>st</sup> range ambiguity**

A full PDiD configuration (i.e. with STC) is then employed using  $\bar{\delta} = 5$  percent for these same three canonical scatterers. Fig. 18 illustrates the result of coherent matching according to the 2<sup>nd</sup> and 3<sup>rd</sup> range ambiguities, which entails using the appropriate STC for each after performing the necessary range alignment. In both of these cases we now observe smearing in both Doppler and range, noting that if STC were not included, little qualitative difference is observed. Moreover, for the top panel the two smeared results reside one range ambiguity away from the  $g = 2$  case for which focused alignment and STC is being performed, and thus the degree of smearing is commensurate for each. In contrast, the bottom panel shows focusing according to the  $g = 3$  range ambiguity, resulting in a doubling in the amount of range smearing of the scatterer from the 1<sup>st</sup> ambiguity, which agrees with the decoherence amplification from (51).

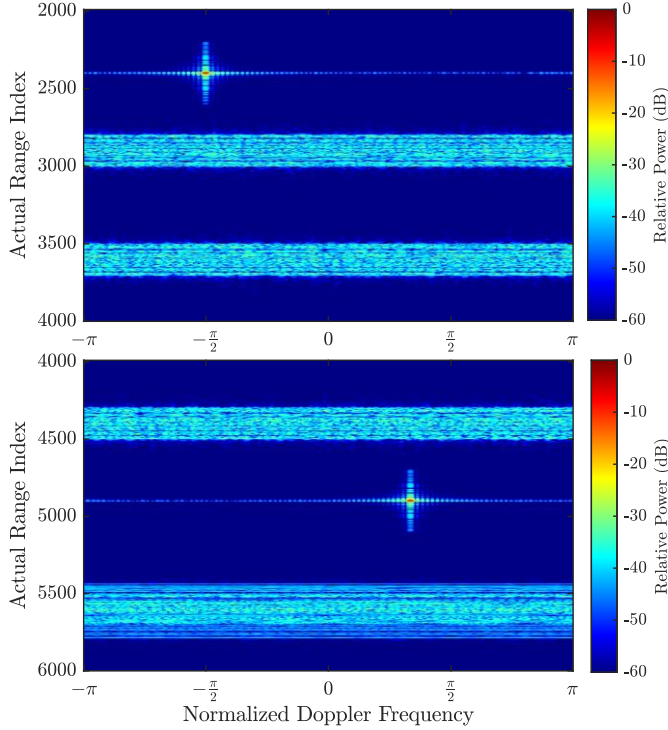


**Fig. 18. Canonical example of 3 scatterers in different range ambiguities for randomly staggered PRIs with STC after range alignment to the (top) 2nd and (bottom) 3rd range ambiguities**

Finally, a Monte Carlo simulation was performed using 2000 independent trials of a random stagger sequence for each value of  $\bar{\delta}$  between 0 and 10 percent. Here a solitary point scatterer is present in the 2<sup>nd</sup> range ambiguity and we examine the response when focusing according to the 1<sup>st</sup> ambiguity (i.e. the degree of range/Doppler smearing), with and without STC. To do so, the standard notions of peak sidelobe level (PSL) and integrated sidelobe level (ISL) are modified to encompass both delay and Doppler. The former then determines the largest peak over the range-folded delay/Doppler span and normalizes by the mainlobe peak when coherent/aligned to the 2<sup>nd</sup> ambiguity. The latter computes the ratio of integrated energy over the range-folded delay/Doppler sidelobe region to the range-folded delay/Doppler mainlobe region (which loses coherency as  $\bar{\delta}$  increases).

Fig. 19 reveals that, as  $\bar{\delta}$  increases, the mean PSL trends downward and the mean ISL trends upward, indicating expanding spread across range/Doppler that is also flattening. Specifically, at  $\bar{\delta}=0$  percent, the impact of spreading due to STC is evident, while the distinction gets smaller as staggering increases. Moreover, for the full PDiD cases (blue traces) the mean PSL reduces by roughly 15 dB and the mean ISL grows by about 28 dB (the latter resulting from division by a progressively shrinking mainlobe response). These trends suggest the prospect of enhanced separability over STC alone, though further examination in the context of realistic scattering is needed to truly quantify the capability.

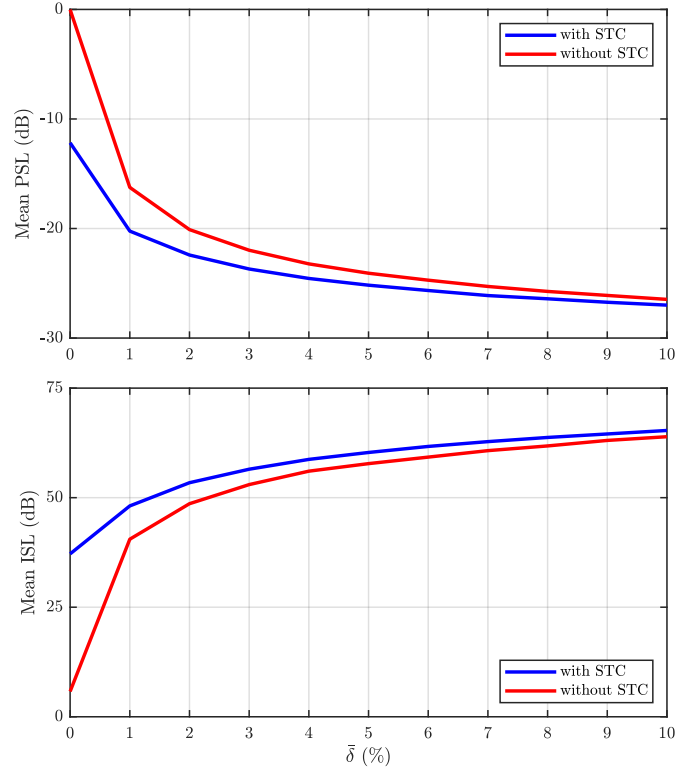


**Fig. 19. Monte Carlo average of modified PSL (top) and ISL (bottom) for a solitary range-folded point scatterer as a function of stagger percentage to illustrate the degree of range/Doppler smearing**

### B. Decoherence Examples for MIMO

To exemplify decoherence in the MIMO context we consider  $P=2$  emitters transmitting  $M=100$  pulses modulated with the same LFM waveform having  $\tau B=50$ , limiting attention to a single range ambiguity (so  $G=1$ ). There are now two distinct point scatterers, one associated with each transmit beam, but otherwise ignoring beamforming effects. Scatterers are still scaled to produce a unity amplitude at the matched point following pulse compression and Doppler processing (when coherent), with specific location details in Table II. Oversampling is again a factor of 4 in range (relative to 3-dB bandwidth) and  $K=10$  in Doppler.

**Table II. Range/Doppler locations (when focused) of canonical MIMO point scatterers**

	Scatterer 1	Scatterer 2
emitter ( $p$ )	1	2
actual range index	1000	500
normalized Doppler	$-\pi/4$	$+\pi/2$

As in the MTA scenarios, we begin with an STC-only assessment (so uniform PRIs) to establish a baseline. Fig. 20 depicts the superimposed responses after pulse compression and Doppler processing according to the 1<sup>st</sup> emitter, with and without STC. The non-STC case (bottom panel) again shows coherent focusing of both scatterers since no means of

separability is being employed. As with MTA, the use of STC to enable MIMO separability [13-18] (top panel) realizes a decoherence in slow-time that translates into smearing across Doppler.

Fig. 21 then depicts the full PDiD configuration (i.e. with STC) using  $\bar{\delta}=0.5$  percent, which is notably an order of magnitude smaller than in the MTA example due to the higher degree of decoherence amplification, per (53) versus (51). Despite this lower staggering we observe a range/Doppler spread that is qualitatively similar to MTA from Fig. 18 (it was found that  $\bar{\delta}=0.7$  percent for MIMO would yield almost identical spread to the MTA case). Consequently, even small staggering can provide meaningful decoherence separability in the MIMO context.

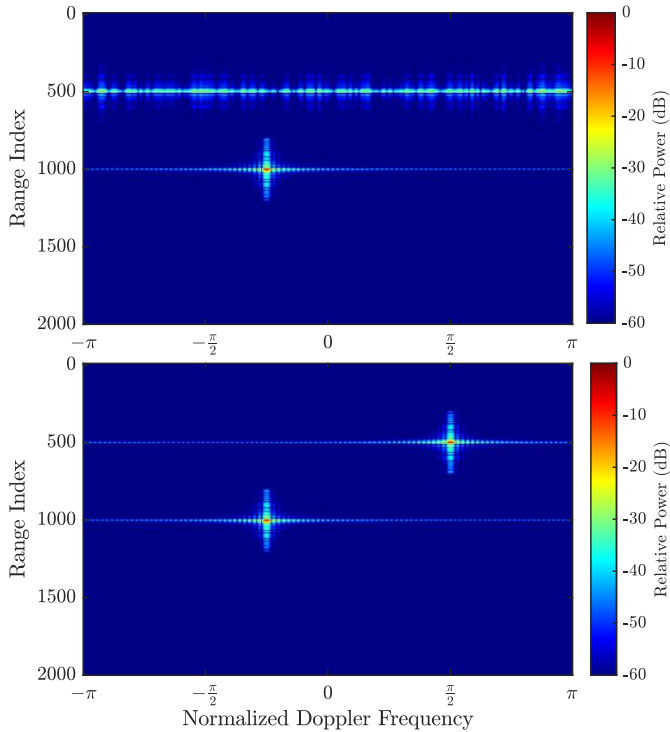


**Fig. 20. Canonical example of 2 scatterers separately illuminated by different MIMO emitters for uniform PRIs, (top) with STC and (bottom) without STC**

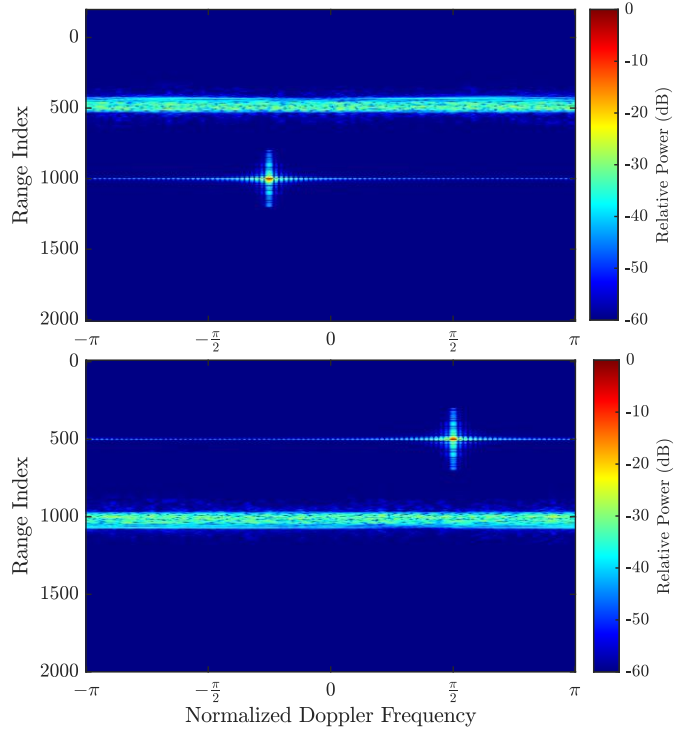


**Fig. 21. Canonical example of 2 scatterers separately illuminated by different MIMO emitters for randomly staggered PRIs and with STC after range alignment to the (top) 1<sup>st</sup> and (bottom) 2<sup>nd</sup> emitter**

Finally, we perform another Monte Carlo simulation using 2000 independent trials of a random stagger sequence for values of  $\bar{\delta}$  between 0 and 1 percent. Here a solitary point scatterer is illuminated by emitter 2 only and we examine the degree of range/Doppler smearing when attempting to receive process according to the stagger sequence (with and without STC) corresponding to emitter 1. The same delay/Doppler modification of PSL and ISL are employed as in the MTA assessment.

As in the MTA case, Fig. 22 shows that increasing  $\bar{\delta}$  causes the mean PSL to trend downward and the mean ISL to trend upward, indicating a clear expansion and flattening of the decoherence spread across range/Doppler. In fact, the  $\bar{\delta}=0$  case here produces exactly the same results as in the MTA plot, which makes sense when considering that those evaluations simply involve a randomization (or not) of  $M$  phase values in the form of STC. However, we now see that the degree of decoherence, as measured by PSL and ISL, is far more sensitive to increasing  $\bar{\delta}$ , with nearly the same change in their values (now roughly  $-12$  dB and  $+22$  dB, respectively, for full PDiD) over only 1 percent as previously occurred over 10 percent for MTA. The benefit of using both staggering and STC is also more pronounced for MIMO. Overall, these trends suggest enhanced separability over STC alone, with the necessity of further examination using realistic scattering.

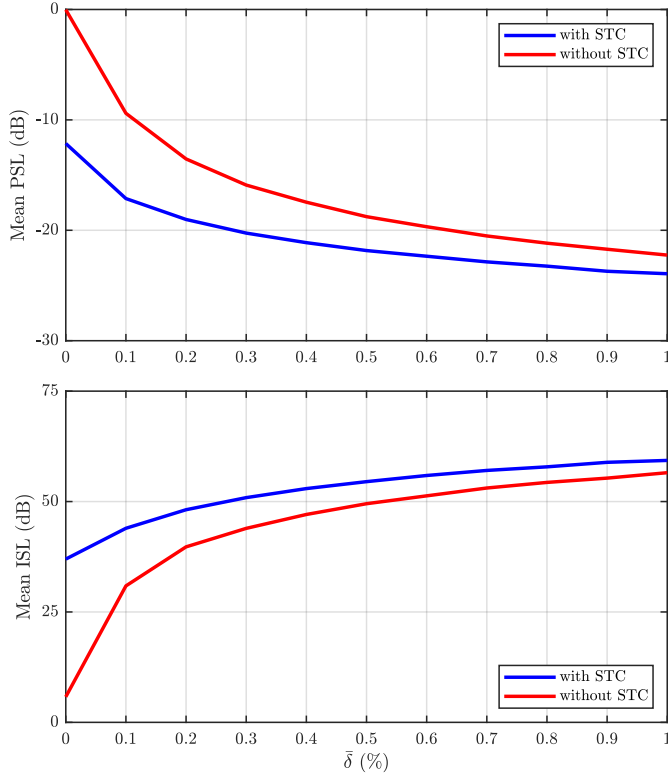


Fig. 22. Monte Carlo average of modified PSL (top) and ISL (bottom) for a MIMO-defocused solitary point scatterer as a function of stagger percentage to illustrate the degree of range/Doppler smearing

## V. CONCLUSIONS

Based on detailed modeling of PRI staggering, and accounting for physically meaningful phenomenology, one can conclude that significant “complexification” arises. Indeed, doing so introduces a variety of factors involving reduction in the range observation interval, decoherence effects and requisite range realignment, and eclipsing considerations. However, there is also the prospect of increased separability and greater design degrees-of-freedom that bear consideration as the radar operating environment itself becomes more congested and complex. We have shown that the expansion of unambiguous Doppler due to random staggering can be predicted on average, and also introduced the notion of a Doppler manifold that encompasses the phase responses collectively induced by staggering and slow-time coding.

The implications to MTA scattering and MIMO configurations have likewise been explored, identifying meaningful operating regimes and associated trade-offs that subsequently arise. While further work is needed to experimentally verify these models, our original thesis of expanding waveform-diverse capabilities through PRI staggering appears to suggest that the PDiD framework does indeed hold promise in that regard, with differing degrees of separability-enabling decoherence amplification associated with the MTA and MIMO modes.

## VI. APPENDIX A

Table III. Definitions of indices, variables, and operators

$m$	Pulse index
$\ell$	Range cell index
$g, \bar{g}, \dot{g}, \tilde{G}$	Range ambiguity indices (bar denotes alignment index)
$p, \bar{p}, \dot{p}$	MIMO emitter index (bar denotes alignment index)
$t$	Fast-time (seconds)
$M$	Number of pulses in a CPI
$K$	Doppler oversampling factor
$N$	Number of quantized Doppler frequency points
$G$	Number of observable range ambiguity intervals
$P$	Number of MIMO emitters
$\tau$	Pulse duration (seconds)
$\chi$	Duty cycle
$v$	Radial velocity of a scatterer (meters/second)
$\lambda$	Wavelength (meters)
$B$	3-dB waveform bandwidth (hertz)
$f_c$	Carrier frequency (hertz)
$f_D$	Doppler frequency (hertz)
$f_{nD}$	Normalized Doppler frequency
$\sigma_n^2$	Noise power (dBm)
$T_m$	$m$ th PRI (seconds)
$T_{\min}, T_{\max}$	Shortest / longest PRI (seconds)
$T_{\text{acc}}(m)$	Accumulated slow-time at start of $m$ th PRI (seconds)
$T_{\text{acc}, \bar{p}}(m)$	Accumulated slow-time at start of $m$ th PRI for $\bar{p}$ th MIMO emitter (seconds)
$T_{\text{avg}}$	Average PRI, same as uniform PRI (seconds)
$\Delta T_m$	$m$ th PRI deviation from uniform (seconds)
$\Delta T_{\text{acc}, \bar{p}}(m)$	Accumulated slow-time deviation at start of $m$ th PRI for $\bar{p}$ th MIMO emitter (seconds)
$\Delta T_{\text{acc}, p, \bar{p}}(m)$	Difference in alignment at start of $m$ th PRI between $\bar{p}$ th and $p$ th MIMO emitters (seconds)
$T_{\text{IS}}$	Time delay of canonical impulse scatterer
$\varepsilon_m$	$m$ th PRI normalized by $T_{\text{avg}}$
$\Delta \varepsilon_m$	$m$ th normalized PRI deviation from uniform
$\varepsilon_{\text{acc}}(m)$	Normalized accumulated slow-time at start of $m$ th PRI

$\Delta\epsilon_{\text{acc}}(m)$	Normalized accumulated PRI deviation at start of $m$ th PRI; also Doppler-to-phase slope deviation
$\Delta\epsilon_{\text{acc}}$	Vector that collects $\Delta\epsilon_{\text{acc}}(m)$ terms
$\Delta\epsilon_{\text{acc},\tilde{G}}$	Vector that collects $\Delta\epsilon_{\text{acc}}(\tilde{G} + m)$ terms for MTA scattering
$\Delta\epsilon_{\text{acc},p}(m)$	Normalized accumulated PRI deviation at start of $m$ th PRI for $p$ th MIMO emitter
$\Delta\epsilon_{\text{acc},p}$	Vector that collects $\Delta\epsilon_{\text{acc},p}(m)$ terms for $p$ th MIMO emitter
$\theta_m, \theta_{\tilde{G}+m}$	Slow-time coding phase at index $m$ , or $\tilde{G} + m$ for MTA (radians)
$\theta_{p,m}$	Slow-time coding phase at index $m$ for $p$ th MIMO emitter (radians)
$\boldsymbol{\theta}, \boldsymbol{\theta}_{\tilde{G}}, \boldsymbol{\theta}_p$	Vector that collects slow-time coding, and MTA and MIMO versions thereof
$\delta$	Symmetric (positive/negative) bound on PRI deviation (seconds)
$\bar{\delta}$	Bound on PRI deviation normalized by $T_{\text{avg}}$ (percentage)
$f_m$	Inverse of $m$ th PRI $T_m$ (hertz)
$\beta$	Factor by which Doppler space is expanded by PRI staggering
$\beta_{\text{mov}}$	Doppler space expansion that captures meaningful mover velocities
$R_{\text{min swath}}$	Smallest observable range swath due to staggering
$R_{\text{max swath}}$	Largest range swath due to staggering
$R_{\text{loss}}$	Amount of range interval lost due to staggering, relative to uniform PRI
$y(m,t)$	Received scattering from $m$ th pulse
$y_{\bar{p}}(m,t)$	Received scattering from $m$ th pulse aligned to $\bar{p}$ th MIMO emitter
$s(t)$	Transmit waveform
$s(t; f_D)$	Fast-time Doppler-shifted version of $s(t)$
$\bar{s}(t; f_D)$	Truncated transmit waveform due to eclipsing
$s_p(t)$	Transmit waveform for $p$ th emitter
$x(t; f_D)$	Doppler-dependent range scattering profile
$\tilde{x}(t; f_D)$	Doppler-dependent range scattering profile shaped by pulse compression
$\tilde{\mathbf{x}}(\ell)$	Slow-time vector of scattering from $\ell$ th range cell after sampling and pulse compression
$\hat{\mathbf{x}}_{\text{DP}}(\ell)$	Estimated Doppler response for $\ell$ th range cell
$\tilde{x}_{m,g}(t; f_D)$	Pulse compressed MTA scattering with range misalignment across PRIs

$\tilde{\mathbf{X}}_g(\ell)$	$M \times N$ matrix of misaligned scattering for $g$ th MTA interval
$\tilde{x}_p(t; f_D)$	Pulse compressed MIMO scattering with range misalignment across PRIs
$\tilde{x}_{\bar{p}}(t; f_D)$	Range aligned scattering for $\bar{p}$ th MIMO emitter
$\tilde{x}_{\bar{p}}(\ell; f_D)$	Range aligned scattering after sampling shaped by pulse compression for $\bar{p}$ th MIMO emitter
$\tilde{\mathbf{x}}_{\bar{p}}(\ell)$	Slow-time vector of range aligned scattering after sampling shaped by pulse compression for $\bar{p}$ th MIMO emitter
$\tilde{\mathbf{a}}_{p,\bar{p}}(\ell; f_D)$	Sampled scattering induced by $p$ th MIMO emitter and range misaligned relative to $\bar{p}$ th emitter's staggering sequence
$\tilde{\mathbf{A}}_{p,\bar{p}}(\ell)$	$M \times N$ matrix of misaligned scattering for $\bar{p}$ th MIMO emitter
$x(T_{\text{IS}})$	Complex scattering for canonical impulse scatterer
$n(m,t)$	Thermal noise for $m$ th pulse
$\tilde{\mathbf{n}}(\ell)$	Vector of sampled noise after pulse compression at $\ell$ th range cell
$\tilde{n}_{\bar{g}}(m,t)$	Pulse compressed noise based on $\bar{g}$ th MTA alignment
$\tilde{\mathbf{n}}_{\bar{g}}(\ell)$	Slow-time vector of sampled and pulse compressed noise based on $\bar{g}$ th MTA alignment
$n_{\bar{p}}(m,t)$	Noise for $\bar{p}$ th MIMO emitter alignment
$\tilde{n}_{\bar{p}}(m,t)$	Pulse compressed noise for $\bar{p}$ th MIMO emitter alignment
$\tilde{\mathbf{n}}_{\bar{p}}(\ell)$	Slow-time vector of sampled and pulse compressed noise based on $\bar{p}$ th MIMO emitter alignment
$z(m,t)$	Pulse compressed received signal
$\mathbf{z}(\ell)$	Slow-time vector of sampled and pulse compressed received signal at $\ell$ th range cell
$z_{\bar{g}}(m,t)$	Pulse compressed received signal based on $\bar{g}$ th MTA alignment
$\mathbf{z}_{\bar{g}}(\ell)$	Slow-time vector of sampled and pulse compressed received signal based on $\bar{g}$ th MTA alignment
$z_{\bar{p}}(m,t)$	Pulse compressed received signal based on $\bar{p}$ th MIMO emitter alignment
$\mathbf{z}_{\bar{p}}(\ell)$	Slow-time vector of sampled and pulse compressed received signal based on $\bar{p}$ th MIMO emitter alignment

$\tilde{\psi}_{\bar{g}}(m, t)$	Pulse compressed scattering based on $\bar{g}$ th MTA alignment subsuming complete slow-time phase
$\tilde{\psi}_{g, \bar{g}}(m, t)$	Pulse compressed scattering for $g$ th MTA interval, subsuming complete slow-time phase, misaligned to $\bar{g}$ th interval
$\tilde{\psi}_{\bar{p}}(m, t)$	Pulse compressed scattering based on $\bar{p}$ th MIMO emitter alignment subsuming complete slow-time phase
$\tilde{\psi}_{p, \bar{p}}(m, t)$	Pulse compressed scattering for $p$ th MIMO emitter, subsuming complete slow-time phase, misaligned to $\bar{p}$ th emitter
$h(t)$	Pulse compression filter for waveform $s(t)$
$h_{\bar{p}}(t)$	Pulse compression filter for $\bar{p}$ th MIMO emitter
$r(t; f_D)$	Doppler-dependent pulse compression filter response
$r_{\bar{p}}(t; f_D)$	Doppler-dependent pulse compression filter response for $\bar{p}$ th MIMO emitter
$c_{p, \bar{p}}(t; f_D)$	Cross-correlation between $p$ th waveform and $\bar{p}$ th pulse compression filter
$r(t - T_{IS})$	Pulse compression response for canonical impulse scatterer
$\mathbf{v}(f_{nD})$	PDiD slow-time steering vector based on normalized Doppler
$\bar{\mathbf{v}}(f_{nD})$	Standard Vandermonde slow-time steering vector
$\mathbf{d}(f_{nD}; \Delta \boldsymbol{\varepsilon}_{acc}, \boldsymbol{\theta})$	Phase deviation slow-time steering vector dependent on PRI staggering and slow-time coding
$\mathbf{V}$	$M \times N$ Doppler-discretized PDiD steering vector matrix
$\mathbf{W}_{DP}$	$M \times N$ Doppler Processing filter bank
$u(f_{nD})$	Zero-referenced Doppler response
$\text{rect}[\tau, T_m]$	Observation interval selection function to account for radar transmit-receive (T-R) switch
$\eta_m(t)$	Generalization of observation interval selection accounting for all $P$ MIMO emitters
$\Gamma_{\bar{g}}\{\mathbf{z}_{\dot{g}}(\ell)\}$	Operator denoting range realignment from $\dot{g}$ to $\bar{g}$ MTA interval (applies in MIMO context from $\dot{p}$ to $\bar{p}$ )
$\odot$	Hadamard product
$\phi_m(f_{nD})$	Complete slow-time phase of $m$ th element of steering vector

## VII. APPENDIX B

Given the zero-referenced Doppler response in (20) and using (7), consider

$$\begin{aligned}
E \left[ \left| \frac{1}{M} u(f_{nD}) \right|^2 \right] &= E \left[ \left| \frac{1}{M} \sum_{m=1}^M e^{-j2\pi f_{nD} \varepsilon_{acc}(m)} \right|^2 \right] \\
&= E \left[ \left| \frac{1}{M} \sum_{m=1}^M e^{-j2\pi f_{nD} [(m-1) + \Delta \varepsilon_{acc}(m)]} \right|^2 \right] \\
&= \frac{1}{M^2} E \left[ \left( \sum_{m=1}^M e^{-j2\pi f_{nD} [(m-1) + \Delta \varepsilon_{acc}(m)]} \right) \right. \\
&\quad \left. \times \left( \sum_{\tilde{m}=1}^M e^{j2\pi f_{nD} [(\tilde{m}-1) + \Delta \varepsilon_{acc}(\tilde{m})]} \right) \right]
\end{aligned} \tag{54}$$

that directly generalizes for (30) or (36) as well. Combining terms from the summations in the last line, we can rewrite (54) as

$$\begin{aligned}
E \left[ \left| \frac{1}{M} u(f_{nD}) \right|^2 \right] &= \frac{1}{M^2} E \left[ \sum_{m=1}^M \sum_{\tilde{m}=1}^M e^{-j2\pi f_{nD} [(m-\tilde{m}) + \Delta \varepsilon_{acc}(m) - \Delta \varepsilon_{acc}(\tilde{m})]} \right] \\
&= \frac{1}{M^2} \sum_{m=1}^M \sum_{\tilde{m}=1}^M e^{-j2\pi f_{nD} (m-\tilde{m})} E \left[ e^{-j2\pi f_{nD} [\Delta \varepsilon_{acc}(m) - \Delta \varepsilon_{acc}(\tilde{m})]} \right] \\
&= \frac{1}{M^2} \sum_{m=1}^M \left[ 1 + \sum_{\tilde{m}=1}^{m-1} e^{-j2\pi f_{nD} (m-\tilde{m})} E \left[ e^{-j2\pi f_{nD} \sum_{q=\tilde{m}}^{m-1} \Delta \varepsilon_q} \right] \right. \\
&\quad \left. + \sum_{\tilde{m}=m+1}^M e^{-j2\pi f_{nD} (m-\tilde{m})} E \left[ e^{+j2\pi f_{nD} \sum_{q=m}^{\tilde{m}-1} \Delta \varepsilon_q} \right] \right]
\end{aligned} \tag{55}$$

where the middle line invokes linearity and the bottom line separates the second summation into components in which  $\tilde{m} = m$ ,  $\tilde{m} < m$ , and  $\tilde{m} > m$ . The new summations in the bottom line exponents of (55) come from the definition  $\Delta \varepsilon_{acc}(m) = \sum_{q=1}^{m-1} \Delta \varepsilon_q$  in (7), with like terms cancelling.

Because the exponent summations in (55) are comprised of independent random stagger offsets, where  $\Delta \varepsilon_q$  is uniformly distributed on  $[-\bar{\delta}, +\bar{\delta}]$ , we can evaluate the remaining expectations to obtain

$$\begin{aligned}
E \left[ e^{-j2\pi f_{\text{ND}} \sum_{q=\tilde{m}}^{m-1} \Delta \varepsilon_q} \right] &= \prod_{q=\tilde{m}}^{m-1} E \left[ e^{-j2\pi f_{\text{ND}} \Delta \varepsilon_q} \right] \\
&= \prod_{q=\tilde{m}}^{m-1} \int_{-\bar{\delta}}^{+\bar{\delta}} \left( \frac{1}{2\bar{\delta}} \right) e^{-j2\pi f_{\text{ND}} \Delta \varepsilon_q} d\Delta \varepsilon_q \\
&= \prod_{q=\tilde{m}}^{m-1} \frac{\sin(2\pi f_{\text{ND}} \bar{\delta})}{2\pi f_{\text{ND}} \bar{\delta}} \\
&= \prod_{q=\tilde{m}}^{m-1} \text{sinc}(2\pi f_{\text{ND}} \bar{\delta}) \\
&= \left[ \text{sinc}(2\pi f_{\text{ND}} \bar{\delta}) \right]^{(m-\tilde{m})}
\end{aligned} \tag{56}$$

for  $\tilde{m} < m$  and

$$\begin{aligned}
E \left[ e^{+j2\pi f_{\text{ND}} \sum_{q=\tilde{m}}^{m-1} \Delta \varepsilon_q} \right] &= \prod_{q=\tilde{m}}^{m-1} E \left[ e^{+j2\pi f_{\text{ND}} \Delta \varepsilon_q} \right] \\
&= \prod_{q=\tilde{m}}^{m-1} \int_{-\bar{\delta}}^{+\bar{\delta}} \left( \frac{1}{2\bar{\delta}} \right) e^{+j2\pi f_{\text{ND}} \Delta \varepsilon_q} d\Delta \varepsilon_q \\
&= \prod_{q=\tilde{m}}^{m-1} \frac{\sin(2\pi f_{\text{ND}} \bar{\delta})}{2\pi f_{\text{ND}} \bar{\delta}} \\
&= \prod_{q=\tilde{m}}^{m-1} \text{sinc}(2\pi f_{\text{ND}} \bar{\delta}) \\
&= \left[ \text{sinc}(2\pi f_{\text{ND}} \bar{\delta}) \right]^{(\tilde{m}-m)}
\end{aligned} \tag{57}$$

for  $\tilde{m} > m$ . Substituting (56) and (57) back into (55) then yields

$$\begin{aligned}
E \left[ \left| \frac{1}{M} u(f_{\text{ND}}) \right|^2 \right] &= \frac{1}{M^2} \sum_{m=1}^M \left[ 1 + \sum_{\tilde{m}=1}^{m-1} e^{-j2\pi f_{\text{ND}} (m-\tilde{m})} \left[ \text{sinc}(2\pi f_{\text{ND}} \bar{\delta}) \right]^{(m-\tilde{m})} \right. \\
&\quad \left. + \sum_{\tilde{m}=m+1}^M e^{-j2\pi f_{\text{ND}} (m-\tilde{m})} \left[ \text{sinc}(2\pi f_{\text{ND}} \bar{\delta}) \right]^{(\tilde{m}-m)} \right] \\
&= \frac{1}{M^2} \left[ M + (M-1)2\cos(2\pi f_{\text{ND}}(1)) \left[ \text{sinc}(2\pi f_{\text{ND}} \bar{\delta}) \right]^1 \right. \\
&\quad \left. + (M-2)2\cos(2\pi f_{\text{ND}}(2)) \left[ \text{sinc}(2\pi f_{\text{ND}} \bar{\delta}) \right]^2 \right. \\
&\quad \left. \dots + (1)2\cos(2\pi f_{\text{ND}}(M-1)) \left[ \text{sinc}(2\pi f_{\text{ND}} \bar{\delta}) \right]^{(M-1)} \right] \\
&= \frac{1}{M} + \frac{2}{M^2} \sum_{m=1}^{M-1} m \cos(2\pi f_{\text{ND}}(M-m)) \left[ \text{sinc}(2\pi f_{\text{ND}} \bar{\delta}) \right]^{(M-m)}
\end{aligned} \tag{58}$$

by Euler's identity and collecting repeated terms, with the final result of (58) shown in (49).

With Figs. 10-14 clearly demonstrating that the expectation result in (49) matches well to the same mean computed over independent random instantiations of staggering, this result can serve as a useful analytical tool to evaluate performance for different parameterizations. Indeed, we could substitute the final line of (58) for  $|u(f)|^2$  in the integrated and extended Doppler sidelobe level (IDSL and EDSL) metrics of (21) and

(22) to understand behavior without need of Monte Carlo trials.

## REFERENCES

- [1] Harnett, L.A., Ravenscroft, B., Blunt, S.D., Allen, C.T., "Experimental evaluation of adaptive doppler estimation for PRI-staggered radar," *IEEE Radar Conf.*, New York City, NY, 21-25 Mar. 2022.
- [2] Kaveh, M., Cooper, G.R., "Average ambiguity function for a randomly staggered pulse sequence," *IEEE Trans. Aerospace & Electronic Systems*, vol. 12, no. 3, pp. 410-413, May 1976.
- [3] Milstein, L.B., "Reduction of eclipsing loss in high PRF radars," *IEEE Trans. Aerospace & Electronic Systems*, vol. AES-14, no. 2, pp. 410-415, Mar. 1978.
- [4] Vergara-Dominguez, L., "Analysis of the digital MTI filter with random PRI," *IEE Proc. F - Radar & Signal Processing*, vol. 140, no. 2, pp. 129-137, Apr. 1993.
- [5] Liu, Z., Wei, X., Li, X., "Aliasing-free moving target detection in random pulse repetition interval radar based on compressive sensing," *IEEE Sensors Journal*, vol. 13, no. 7, pp. 2523-2534, July 2013.
- [6] Zhu, J., Zhao, T., Huang, T., Zhang, D., "Analysis of random pulse repetition interval radar," *IEEE Radar Conference*, Philadelphia, PA, 2-6 May 2016.
- [7] Long X., Li, K., Tian, J., Wang, J., Wu, S., "Ambiguity function analysis of range agile frequency and PRI agile signals," *IEEE Trans. Aerospace & Electronic Systems*, vol. 57, no. 1, pp. 382-396, Feb. 2021.
- [8] Richards, M.A., Scheer, J.A., Holm, W.A., eds., *Principles of Modern Radar: Basic Principles*. SciTech Publishing, Raleigh, NC, 2010.
- [9] Blunt, S.D., Mokole, E.L., "On overview of radar waveform diversity," *IEEE Aerospace & Electronic Systems Mag.*, vol. 31, no. 11, pp. 2-42, Nov. 2016.
- [10] Hovanessian, S.A., "An algorithm for calculation of range in a multiple PRF radar," *IEEE Trans. Aerospace & Electronic Systems*, vol. 12, no. 2, pp. 287-290, March 1976.
- [11] Trunk, G., Brockett, S., "Range and velocity ambiguity resolution," *IEEE National Radar Conf.*, pp. 146-149, Apr. 1993.
- [12] Trunk, G., Kim, M.W., "Ambiguity resolution of multiple targets using pulse-doppler waveforms," *IEEE Trans. Aerospace & Electronic Systems*, vol. 30, no. 4, pp. 1130-1137, Oct. 1994.
- [13] Mecca, V.F., Ramakrishnan, D., Krolik, J.L., "MIMO radar space-time adaptive processing for multipath clutter mitigation," *IEEE Sensor Array & Multichannel Processing Workshop*, Waltham, MA, July 2006.
- [14] van Rossum, W., Anitori, L., "Doppler ambiguity resolution using random slow-time code division multiple access MIMO radar with sparse signal processing," *IEEE Radar Conf.*, Oklahoma City, OK, Apr. 2018.
- [15] Madsen, N., Cao, S., "Slow-time waveform design for MIMO GMTI radar using CAZAC sequences," *IEEE Radar Conf.*, Oklahoma City, OK, Apr. 2018.
- [16] Anitori, L., Ender, J., "Waveform design for sparse signal processing in radar," *IEEE Radar Conf.*, Atlanta, GA, May 2021.
- [17] Rabideau, D.J., "Doppler-offset waveforms for MIMO radar," *IEEE Radar Conf.*, Kansas City, MO, May 2011.
- [18] Rabideau, D.J., "MIMO radar waveforms and cancellation ratio," *IEEE Trans. Aerospace & Electronic Systems*, vol. 48, no. 2, pp. 1167-1178, Apr. 2012.
- [19] Van Trees, H.L., *Optimum Array Processing*, John Wiley & Sons, New York, NY, 2002.
- [20] Kennedy, M.C., O'Hagan, A., "Bayesian calibration of computer models," *Journal of the Royal Statistical Society: Series B (Statistical Methodology)*, vol. 63, part 3, pp. 425-464, 2001.
- [21] Oliver, T.A., Terejanu, G., Simmons, C.S., Moser, R.D., "Validating predictions of unobserved quantities," *Computer Methods in Applied Mechanics & Engineering*, vol. 283, pp. 1310-1335, Jan. 2015.
- [22] *Journal on Uncertainty Quantification*, SIAM/ASA, 2013-present.
- [23] Jones, C.C., Mohr, C.A., McCormick, P.M., Blunt, S.D., "Complementary frequency modulated radar waveforms and optimised receive processing," *IET Radar, Sonar & Navigation*, vol. 15, no. 7, pp. 708-723, Apr. 2021.

- [24] Mohr, C.A., McCormick, P.M., Topliff, C.A., Blunt, S.D., Baden, J.M., "Gradient-based optimization of PCFM radar waveforms," *IEEE Trans. Aerospace & Electronic Systems*, vol. 57, no. 2, pp. 935-956, Apr. 2021.
- [25] Owen, J., Mohr, C., Ravenscroft, B., Blunt, S., Kirk, B., Martone, A., "Real-time experimental demonstration and evaluation of open-air sense-and-notch radar," *IEEE Radar Conf.*, New York City, NY, Mar. 2022.
- [26] Jones, C.C., Gannon, Z.E., DePardo, D., Owen, J.W., Blunt, S.D., Allen, C.T., Kirk, B.H., "Development & experimental assessment of robust direction finding and self-calibration," *IEEE Radar Conf.*, New York City, NY, Mar. 2022.
- [27] Jones, C.C., Harnett, L.A., Mohr, C.A., Blunt, S.D., Allen, C.T., "Structure-based adaptive radar processing for joint clutter cancellation and moving target estimation," *IEEE Intl. Radar Conf.*, Washington, DC, Apr. 2020.
- [28] Harnett, L., Hemmingsen, D., McCormick, P.M., Blunt, S.D., Allen, C., Martone, A., Sherbondy, K., Wikner, D., "Optimal and adaptive mismatch filtering for stretch processing," *IEEE Radar Conf.*, Oklahoma City, OK, Apr. 2018.
- [29] Richards, M.A., *Fundamentals of Radar Signal Processing*, 2<sup>nd</sup> ed., McGraw-Hill, New York, NY, 2014.
- [30] Levanon, N., Mozeson, E., *Radar Signals*. Hoboken, NJ: John Wiley Sons, Inc., 2004.
- [31] Skolnik, M., *Radar Handbook*, 3<sup>rd</sup> ed., McGraw-Hill, New York, NY, 2008, pp. 4.40-4.43.
- [32] Klein, A.M., Fujita, M.T., "Detection performance of hard-limited phase-coded signals," *IEEE Trans. AES*, vol. AES-15, no. 6, pp. 795-802, Nov. 1979.
- [33] Blunt, S.D., Cook, M., Jakabosky, J., de Graaf, J., Perrins, E., "Polyphase-coded FM (PCFM) radar waveforms, part I: implementation," *IEEE Trans. Aerospace & Electronic Systems*, vol. 50, no. 3, pp. 2218-2229, July 2014.
- [34] Hartnett, M.P., Clancy, J.T., Denton, R.J., "Utilization of a nonrecurrent waveform to mitigate range-folded spread doppler clutter: application to over-the-horizon radar," *Radio Science*, vol. 33, no. 4., pp. 1125-1133, July/Aug. 1998.
- [35] Clancy, J., Bascom, H., Hartnett, M., "Mitigation of range folded clutter by a nonrecurrent waveform," *IEEE Radar Conf.*, Waltham, MA, pp. 79-83, Apr. 1999.
- [36] Lin, F.-L., Steiner, M., "New techniques for radar coherent range ambiguity resolution," *IEEE Radar Conf.*, Atlanta, GA, May 2001.
- [37] Lee, W.W., "Radar space-time processing for range-folded spread-doppler clutter mitigation," PhD dissertation, Duke University, 2011.
- [38] Steiner, M., Kretschmer, F.F., "Missing radar pulse clutter processing," *IEEE Aerospace & Electronic Systems Magazine*, vol. 6, no. 5, pp. 23-27, May 1991.
- [39] Villano, M., Krieger, G., Moreira, A., "Staggered SAR: high-resolution wide-swath imaging by continuous PRI variation," *IEEE Trans. Geoscience & Remote Sensing*, vol. 52, no. 7, pp. 4462-4479, July 2014.
- [40] Blunt, S.D., Metcalf, J., Jakabosky, J., Stiles, J., Himed, B., "Multi-waveform space-time adaptive processing," *IEEE Trans. Aerospace & Electronic Systems*, vol. 53, no. 1, pp. 385-404, Feb. 2017.
- [41] Kolodziej, K.E., Brigham, G.A., Harger, M.A., Janice, B.A., Sands, A.I., Weiner, I., Wolfe, P.-F.W., Doane, J.P., Perry, B.T., "Scalable array technologies for converged-RF applications," *IEEE Radar Conf.*, New York City, NY, Mar. 2022.
- [42] Cox, C.H., Ackerman, E.I., "Review of radar system needs, and performance of techniques, for STAR," *IEEE Radar Conf.*, New York City, NY, Mar. 2022.
- [43] Collins, T., Atkins, P., "Nonlinear frequency modulation chirps for active sonar," *IEE Proc. Radar, Sonar & Navigation*, vol. 146, no. 6, pp. 312-316, Dec. 1999.
- [44] Jakabosky, J., Blunt, S.D., Himed, B., "Spectral-shape optimized FM noise radar for pulse agility," *IEEE Radar Conf.*, Philadelphia, PA, May 2016.
- [45] Heintzelman, M.B., Kramer, T.J., Blunt, S.D., "Experimental evaluation of super-Gaussian-shaped random FM waveforms," *IEEE Radar Conf.*, New York City, NY, Mar. 2022.



**Shannon D. Blunt** (S'96–M'02–SM'07–F'16) is the Roy A. Roberts Distinguished Professor of Electrical Engineering & Computer Science (EECS) at the University of Kansas (KU), Director of the KU Radar Systems & Remote Sensing Lab (RSL), and Director of the Kansas Applied Research Lab (KARL). He received a PhD in electrical engineering from the University of Missouri in 2002, and from 2002 until 2005 he was with the Radar Division of the U.S. Naval Research Laboratory in Washington, D.C. He received an AFOSR Young Investigator Award in 2008, the IEEE/AESS Nathanson Memorial Radar Award in 2012, was named a Fellow of the IEEE in 2016, was appointed to the U.S. President's Council of Advisors on Science & Technology (PCAST) in 2019, and received the 2020 IET Radar, Sonar & Navigation Premium Award, along with multiple teaching awards. He has over 200 refereed journal, conference, and book chapter publications, and 18 patents/patents-pending. He co-edited the books *Principles of Waveform Diversity & Design* (2010) and *Radar & Communication Spectrum Sharing* (2018).

He has served as a subject matter expert on radar spectrum for DARPA, the Air Force's S&T 2030 Initiative, the National Spectrum Consortium, the Office of the Under Secretary of Defense for Research & Engineering (OUSD(R&E)), and the White House Office of Science & Technology Policy (OSTP). He served as Chair of the IEEE/AESS Radar Systems Panel and on the AESS Board of Governors. He is Editor-in-Chief for *IEEE Transactions on Radar Systems*, is on the Editorial Board for *IET Radar, Sonar & Navigation*, and served in different editorial roles for *IEEE Transactions on Aerospace & Electronic Systems*. He has been General Chair or Technical Chair for multiple *IEEE Radar Conferences* and serves on the Program Committee for the *MSS Tri-Service Radar Symposium* series. He was also Chair of NATO SET-179 research task group on "Dynamic Waveform Diversity & Design".



**Lumumba A. Harnett** (S'12-GS'14-M'22) received the bachelor's degree (magna cum laude) in electrical engineering in 2014 from Hampton University, Hampton, VA, USA, and the master's and Ph.D. degrees in electrical engineering from the University of Kansas (KU) in 2018 and 2022, respectively. While at KU he was a Chancellor's Doctoral Fellow and a National Science Foundation (NSF) Graduate Research Fellow, and was affiliated with the KU Radar Systems Laboratory (RSL). From 2020 to 2022, he was a Principal Systems Engineer with Northrup Grumman Missions Systems in Baltimore, MD, USA and he is currently a Senior Signal Processing Engineer at Leidos in Arlington, VA, USA.



**Brandon Ravenscroft** (S'15-GS'16) received the B.S. in electrical engineering in 2015 from the University of Kansas (KU), where he is currently working toward the Ph.D. in electrical engineering. He received the 2020 IET Radar, Sonar & Navigation Premium Award and competed as a top 5 finalist in the best student paper competitions at the 2017

IET International Radar Conference in Belfast, UK, and the 2019 IEEE Radar Conference in Boston, MA, USA. His research interests include radar signal processing, cognitive radar, waveform design and radar/communication spectrum cohabitation. He will soon be joining Johns Hopkins University - Applied Physics Lab in Laurel, MD.



**Rachel J. Chang** (S'19-GS'21) received the B.S. degree in Electrical Engineering from the University of Kansas in 2020, where she is currently working toward a M.S. degree in electrical engineering. Since 2019, she has been affiliated with the KU Radar Systems Laboratory. Her research interests include radar signal processing, waveform design, and pulse-

Doppler radar.



**Christopher T. Allen** (S'79-M'83-SM'95) is a Professor in the EECS department at The University of Kansas. Chris' research areas include radar systems and remote sensing as well as photonic sensors. He has over 140 refereed publications, 18 patents, and is a senior member of the IEEE. Prior to joining KU in 1994, Prof. Allen was a Senior Staff Engineer at the NNSA/DOE

Kansas City Plant, Kansas City, MO (1990-1994) working in the areas of high-speed digital design, radar systems analysis, and multi-chip module development. Preceding this (1984-1990), he was a Senior Member of the Technical Staff at Sandia National Laboratories in Albuquerque, NM where he developed high-speed digital systems for advanced synthetic-aperture radar systems and also performed system design and analysis on a variety of radar programs. Dr. Allen received the BS, MS, and PhD degrees in electrical engineering from the University of Kansas in Electrical Engineering in 1980, 1982, 1984.



**Patrick M. McCormick** (S'12-M'18) received the B.S. degree in mechanical engineering, the B.S. in electrical engineering, and the Ph.D. degree in electrical engineering from the University of Kansas, Lawrence, KS, USA, in 2008, 2013, and 2018, respectively. From 2018 to 2021, he served as a research electronics engineer

with the Air Force Research Laboratory - Sensors Directorate, Wright-Patterson AFB, OH. In 2021, he began his current position as an Assistant Professor / Assistant Scientist at the University of Kansas in the Electrical Engineering and Computer Science department. He has multiple refereed journal publications, conference papers, book chapters, and patents in the areas of waveform diversity and design, adaptive receive signal processing, and radar/communication spectrum sharing. Dr. McCormick has received numerous awards and honors including the 2018 Robert T. Hill Best Dissertation Award; PhD EE with honors in May 2018; University of Kansas Electrical Engineering and Computer Science Department Nominee for Outstanding Doctoral Researcher; 1st Place in the 2018 IEEE Radar Conference Student Paper Competition; and 3rd place in the 2016 IEEE Radar Conference Student Paper Competition.